Inorganic Chemistry

Article

pubs.acs.org/IC

Hydride Binding to the Active Site of [FeFe]-Hydrogenase

Petko Chernev,[†,∇] Camilla Lambertz,[‡,∇,∥] Annika Brünje,[‡] Nils Leidel,[†] Kajsa G. V. Sigfridsson,[†,○] Ramona Kositzki,[†] Chung-Hung Hsieh,[⊥] Shenglai Yao,[#] Rafael Schiwon,[§] Matthias Driess,[#] Christian Limberg,[§] Thomas Happe,[‡] and Michael Haumann*[,†]

[†]Institute for Experimental Physics, Free University Berlin, 14195 Berlin, Germany

[‡]Institute for Biochemistry of Plants, Department of Photobiotechnology, Ruhr-University Bochum, 44801 Bochum, Germany

[⊥]Department of Chemistry, Texas A&M University, College Station, Texas 77843, United States

[#]Department of Chemistry, Technical University Berlin, 10623 Berlin, Germany

[§]Department of Chemistry, Humboldt University Berlin, 12489 Berlin, Germany

Supporting Information

ABSTRACT: [FeFe]-hydrogenase from green algae (HydA1) is the most efficient hydrogen (H_2) producing enzyme in nature and of prime interest for (bio)technology. Its active site is a unique six-iron center (H-cluster) composed of a cubane cluster, $[4Fe4S]_H$, cysteine-linked to a diiron unit, $[2Fe]_H$, which carries unusual carbon monoxide (CO) and cyanide ligands and a bridging azadithiolate group. We have probed the molecular and electronic configurations of the H-cluster in functional oxidized, reduced, and super-reduced or CO-inhibited HydA1 protein, in particular searching for intermediates with iron-hydride bonds. Site-selective X-ray absorption and emission spectroscopy were used to distinguish between low- and high-spin iron sites in the two subcomplexes of the H-cluster. The experimental methods and spectral simulations were calibrated using synthetic model complexes with ligand variations and bound hydride species. Distinct X-ray spectroscopic signatures of electronic excitation or decay transitions in $[4Fe4S]_H$ and $[2Fe]_H$ were obtained, which were quantitatively reproduced by density functional theory calculations, thereby leading to specific H-cluster model structures. We show that iron-hydride bonds are absent in the reduced state, whereas only in the super-reduced state, ligand rotation facilitates hydride binding presumably to the Fe−Fe bridging position at $[2Fe]_H$. These results are in agreement with a catalytic cycle involving three main intermediates and at least two protonation and electron transfer steps prior to the H_2 formation chemistry in [FeFe]-hydrogenases.

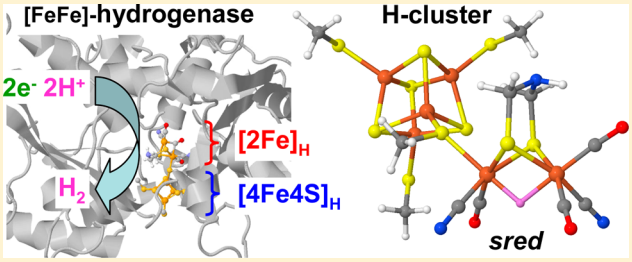

INTRODUCTION

Hydrogen (H_2) is expected to play a prominent role as a sustainable fuel in a future economy based on renewable energy resources.[1] At present, a major challenge for industrial-scale H_2 production is the development of inexpensive and durable catalysts, which do not contain rare noble metals such as platinum.[2] Nature offers efficient H_2-formation catalysts in the form of [FeFe]-hydrogenase enzymes, which use protein-bound iron to perform the chemistry.[3,4] Their active site, termed the H-cluster, may serve as a blueprint for novel synthetic catalysts,[5−8] and hydrogenase-containing organisms could even be employed directly in biotechnology.[9] However, both applications require fundamental understanding of the catalysts' reaction mechanism. How redox transitions are orchestrated with protonation reactions to yield metal-hydride intermediates on the way to H_2 production is a key question in biological and synthetic hydrogen chemistry at transition metal centers.[10−13]

The [FeFe]-hydrogenase (HydA1) from green algae (e.g., *Chlamydomonas reinhardtii*) is considered as the minimal unit of biological H_2 production.[14] It contains only the H-cluster and no further iron−sulfur clusters unlike bacterial enzymes and therefore is a superior target for a focused search for iron-hydride intermediates at the active site using spectroscopy. Protein crystallography has revealed that the six iron atoms of the H-cluster are arranged in a canonical cubane-type iron−sulfur cluster, $[4Fe4S]_H$, which is linked via the thiol group of a cysteine amino acid to a diiron active site, $[2Fe]_H$.[15,16] The two iron atoms of $[2Fe]_H$, in proximal (Fe_p) or distal (Fe_d) positions relative to $[4Fe4S]_H$, carry biologically atypical carbon monoxide (CO) and cyanide (CN^-) ligands.[17,18] In addition, an Fe−Fe bridging group is present in $[2Fe]_H$, which has been assigned as an azadithiolate moiety (adt = $(SCH_2)_2NH$) based on electron paramagnetic resonance spectroscopy (EPR) experiments.[19] The recent demonstration of functional reconstitution of apo-HydA1 protein containing only the $[4Fe4S]_H$ cluster[20] using a synthetic adt-containing diiron complex proved the presence of the adt nitrogen base.[21,22] An example of an H-cluster crystal structure for bacterial [FeFe]-

Received: August 31, 2014
Published: November 4, 2014

   dx.doi.org/10.1021/ic502047q | Inorg. Chem. 2014, 53, 12164−12177

hydrogenase, revealing the overall geometry of the cofactor, is shown in Figure 1.

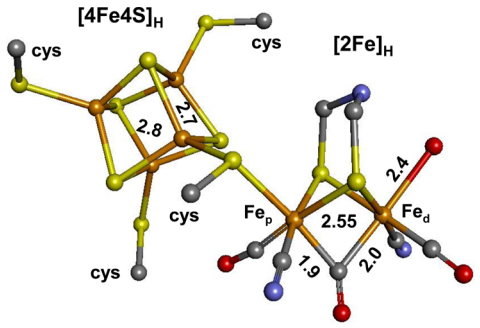

Figure 1. Crystal structure of the H-cluster in [FeFe]-hydrogenase. The structure is for CpI from *Clostridium pasteurianum*, PDB entry 3C8Y,[105] 1.4 Å resolution. The O atom of the bridging ligand in $[2Fe]_H$ here was replaced by an N atom to yield an azadithiolate (adt) group,[21,22] some interatomic distances (in Å) are indicated, Fe_p and Fe_d denote the irons of $[2Fe]_H$ in proximal or distal positions relative to $[4Fe4S]_H$, and cys marks cysteine amino acid residues. The structure corresponds to air-oxidized protein showing an oxygen species at Fe_d. Protons (i.e., at the adt-N) were not resolved by X-ray crystallography and therefore are omitted.

The assembly of the H-cluster during the maturation of [FeFe]-hydrogenases involves three accessory proteins (HydE,F,G).[23−31] Today, procedures for the preparation of highly active natively or in vitro matured HydA1 protein are readily available.[32−35] Dedicated methods for the steady-state population of defined redox intermediates of the H-cluster, such as the oxidized, (singly) reduced, and so-called super- (doubly) reduced states have been reported.[36−39] On the basis of crystallographic, spectroscopic, and molecular biology studies, the involvement of open coordination sites at $[2Fe]_H$ in certain states, as probed for example by inhibitors of the H_2 chemistry such as CO, formaldehyde, or O_2,[40−42] and of the dithiolate bridge[43] and the protein matrix,[32] in protonation processes at the active site has been suggested.[42,44] Reaction intermediates in the catalytic cycle with hydrogen species bound to iron have been proposed accordingly.[36,37,45,46] Experimental evidence for iron-hydride bonds at the H-cluster, however, so far has been lacking.

The combination (XAE) of high-resolution X-ray absorption (XAS) and narrow-band emission (XES) spectroscopy at modern synchrotron radiation sources is a sensitive tool for detection of structural and electronic changes at metal centers.[47−49] XAE experiments facilitate site-selective spectroscopic discrimination of metal sites with different spin states, oxidation levels, and coordination environments in heterogeneous materials.[50−59] We have recently demonstrated that XAE allows for specific discrimination of the $[4Fe4S]_H$ and $[2Fe]_H$ units of the H-cluster in HydA1.[60] The pre-K-edge region of the XAS spectrum probes core-to-valence (c2v) electronic excitations (e.g., 1s → 3d) to unoccupied molecular orbitals (MOs), whereas the $K\beta_{2,5}$ emission region in the XES spectrum monitors the complementary reverse process, valence-to-core (v2c) electronic decay (e.g., 3d → 1s) from occupied MOs. Respective c2v and v2c spectra can be accurately calculated using quantum chemical approaches (density functional theory, DFT), revealing the underlying molecular structures and electronic configurations.[60−63] Both sets of XAE spectra have been shown to be sensitive to structural changes at iron sites and in particular are altered due to iron-hydride bond formation.[48,64,65]

Here, we have obtained site-selective XAE spectra for $[4Fe4S]_H$ and $[2Fe]_H$ in the oxidized (*ox*), reduced (*red*), super-reduced (*sred*), and CO-treated (*CO*) states of the H-cluster in purified HydA1 protein from *C. reinhardtii*. Synthetic crystallized model complexes served as benchmarks for iron-hydride bond detection by XAE and calibration of the analysis methods. DFT calculations assigned differences in molecular and electronic configurations of the H-cluster states and yielded specific model structures. This has provided the first evidence for an iron-hydride intermediate of the active site in the hydrogen formation cycle.

MATERIALS AND METHODS

Protein Sample Preparation. *C. reinhardtii* [FeFe]-hydrogenase HydA1 was overexpressed in *Clostridium acetobutylicum* (strain ATCC 824), purified via Strep-Tag affinity chromatography with O_2-free buffer (100 mM Tris/HCl (pH 8.0), 2 mM sodium dithionite (NaDT)), and frozen in gastight cups at −80 °C in the same buffer supplemented with 10% (v/v) glycerol as previously described.[33,42,60] HydA1 protein from several purifications with similar specific activities was pooled. Enzyme purification, protein up-concentration to up to ∼2 mM (Amicon Ultracel 10 kDa, Millipore), and protein treatments were performed under strictly anoxic conditions in an anaerobic tent. All buffers and solutions were made anoxic by degassing prior to use. After each freeze/thaw step and after up-concentration of protein, specific activities were determined to ensure preservation of full catalytic activity. HydA1 samples were treated to populate the oxidized (*ox*), reduced (*red*), super-reduced (*sred*), and carbon monoxide inhibited (*CO*) states of the H-cluster after protein up-concentration as described below, filled into sample holders for XAE, and immediately frozen in liquid nitrogen, following established procedures.[36,60,66] HydA1 *red*: protein was isolated in the presence of 2 mM NaDT as described above. According to previous estimates,[36,67] these samples contained the *red* state in at least 70% quantities. HydA1 *ox*: HydA1 *red* (∼1 mM) samples (∼30 μL) were mixed in PCR tubes with thionine (∼2 mM) in TPW buffer, added in 1−2 μL aliquots until no further rapid color change of the added thionine from blue (oxidized) to colorless (reduced) was observed, which indicated maximal oxidation of HydA1.[68] HydA1 *CO*: HydA1 *red* samples (∼1 mM) were flushed with carbon monoxide gas (4.7 grade), moistured by passing through anoxic buffer to avoid sample dehydration, for 60 min in a PCR tube placed in a gastight cup. HydA1 *sred*: Protein samples were fully reduced by incubation with excess NaDT or flushing with H_2 gas. $NaDT_{excess}$: HydA1 *red* samples (∼1 mM) were mixed with a stock solution of NaDT so that the final NaDT concentration in the samples was ∼20 mM, directly filled into XAE sample holders, and frozen in liquid nitrogen. H_2: HydA1 *red* (∼1 mM) samples were flushed with H_2 gas (5.0 grade), moistured by passing through anoxic buffer to avoid sample dehydration, for 15−20 min in a PCR tube placed in a gastight cup. The apoprotein of HydA1 (apo-HydA1) containing only the $[4Fe4S]_H$ unit was obtained by protein overexpression in *E. coli* strain BL21 DE3 DiscR using a pET plasmid lacking the respective maturases (HydE, HydG, HydF) for assembly of the active H-cluster structure.[22,35]

Synthetic Iron Model Complexes. Six crystallized iron complexes (coordinates are given in the Supporting Information, Table S1) were synthesized following reported procedures: $\mathbf{1}_{FeCO}$, $(CO)_3Fe[cpdO(tms)_2]$ (cpd = η^4-cyclopentadienone, tms = trimethylsilyl) and $\mathbf{1}_{FeH}$, $H(CO)_3Fe[cpdOH(tms)_2]$;[69,70] $\mathbf{2}_{2Fe}$, $(\mu$-pdt$)[Fe(CO)_2(PMe_3)]_2$ (pdt = propane dithiolate) and $\mathbf{2}_{2Fe\mu H}$, $(\mu$-H$)(\mu$-pdt$)[Fe(CO)_2(PMe_3)]_2$;[71] $\mathbf{3}_{2Fe2\,\mu S}$, $(\mu S)_2[Fe(dk)]_2$ (dk = ß-diketiminate) and $\mathbf{3}_{2Fe2\,\mu H}$, $(\mu H)_2[Fe(dk)]_2$ (complexes **3** were derived in analogy to ref 72; further details of the synthesis will be given in a forthcoming publication). Powder samples of complexes were diluted with solid boron nitrite powder (1:10 w/w), transferred to XAE sample holders, and immediately frozen in liquid nitrogen.

dx.doi.org/10.1021/ic502047q | *Inorg. Chem.* 2014, 53, 12164−12177

X-ray Spectroscopy. XAE data at the Fe K-edge were collected at the three-undulator beamline ID26 at the European Synchrotron Radiation Facility (ESRF, Grenoble, France) as previously.[50,60,65,73] Samples were held in a liquid-He cryostat at 20 K. The excitation energy was set by an Si[311] double-crystal monochromator (energy bandwidth ~0.2 eV). The spot size on the samples was set by slits (~0.2 mm vertical × ~0.5 mm horizontal). The incident X-ray flux at the Fe K-edge at the sample position was estimated as ~2×10^{12} photons s^{-1}. Conventional Fe K-edge absorption spectra were collected by monitoring the total X-ray fluorescence (>95% Kα emission after the Mn filter foil) with a scintillation detector (~20 cm^2 area, placed at 90° to the incident X-rays and at ~1 m to the sample) shielded by 10 μm Mn foil against scattered X-rays using the rapid scan mode of ID26 within 5−15 s. A vertical-plane Rowland-circle spectrometer and an avalanche photodiode (APD) detector were used for monitoring the Kß X-ray fluorescence. An energy bandwidth of ~1.0 eV at the Fe Kß fluorescence lines was achieved using the Ge[620] Bragg reflections of five spherically bent Ge wafers (R = 1000 mm). The energy axis of the monochromator was calibrated (±0.1 eV) using the K-edge spectrum of an Fe metal foil (fitted reference energy 7112 eV in the first derivative spectrum). The energy axis of the emission spectrometer was calibrated (±0.1 eV) using a fit to the elastic scattering peak of the energy-calibrated excitation beam. Kß main line (Kß′ and $Kß_{1,3}$) and satellite line ($Kß_{2,5}$) emission spectra were collected on separate sample spots within 10−20 s (energy steps of 0.3 eV) with overlapping spectral ranges for normalization. Up to 20 scans in the $Kß_{2,5}$ region were averaged. Rapid-scan Fe K-edge absorption spectra were measured in 5−15 s using parallel Kß emission and total fluorescence detection (averaging of up to ~100 scans, ≤5 scans per sample spot; the total number of averaged scans was adjusted so that a similar signal-to-noise ratio of XANES spectra resulted for detection at different Kß emission energies corresponding to different emission intensities). For collection of resonant inelastic X-ray scattering (RIXS) data, the emission detection energy was varied over the Kß region in 0.3 eV steps, and for each energy a rapid monochromator scan (~1 s duration, 0.1 eV per data point) in the pre-edge absorption region (7110−7120 eV) was carried out (~2 min total X-ray exposure of samples). A rapid shutter blocked the incident X-rays during emission spectrometer movements. RIXS data were evaluated using in-house Matlab (Mathsoft) tools.

XAE Data Processing. Averaged K-edge absorption spectra were normalized,[74] and the pre-edge features were isolated using the software XANDA[75] by subtraction of a smooth baseline spline curve, which accounted for the extrapolated main edge rise background (see Figure 4B). After background subtraction, the resulting c2v spectra of HydA1 were smoothed over data points within 0.7 eV using the Savitzky-Golay algorithm and a third-order polynomial. Kß emission line spectra were normalized to unity area in the 7035−7120 eV energy region, by shifting of the spectra so that the average amplitude of the last 5 high-energy data points (1.5 eV) was zero, i.e., subtracting a small offset level from the spectra. A background curve, representing the high-energy tail of the $Kß_{1,3}$ main line emission, was subtracted from the $Kß_{2,5}$ (v2c) spectra (see Figures 3B and S3). Normalized $Kß^{2,5}$ lines of HydA1 protein samples were smoothed over data points within 3.3 eV using the Savitzky-Golay algorithm and a third-order polynomial before (Figures 5, 8) or after (Figure S3) background subtraction, which only marginally affected the spectral shape of $Kß_{2,5}$ difference spectra. No data smoothing was involved in the processing of the XAE spectra of the model compounds. Apparent energies of electronic transitions into or from molecular orbitals with iron 3d character were determined from second derivatives of pre-edge absorption or $Kß_{2,5}$ emission spectra as explained in the legend of Figures S6 and S7.

Density Functional Theory Calculations. Geometry-optimization of H-cluster model structures and spin-unrestricted single-point calculations for simulation of X-ray spectra were carried out with the DFT program package ORCA.[50] The BP86 exchange correlation functional,[76,77] a triple-ζ valence plus double polarization (TZVPP) basis set,[78] and the COSMO solvation model[79] (ε = 4) were used as previously.[50,60,65,73] Initial H-cluster model structures for DFT were constructed using crystal structures of bacterial [FeFe]-hydrogenases as templates.[16,80] The cysteine side chains of the thiol ligands to $[4Fe4S]_H$ were truncated to S-CH_3 groups, and in the geometry optimizations, the carbon atoms of the four S-CH_3-groups and Fe_p were fixed at their crystallographic positions. The total spin multiplicity (M = 2S + 1) of the H-cluster system was 1 or 2, depending on the number of electrons. The total charge of the H-cluster models was −4 or −3 for unprotonated or protonated *red* structures, −3 for *ox* (protonation state as for unprotonated *red*), and −4 or −5 for protonated or unprotonated *sred* structures. A broken-symmetry approach[81] was used as implemented in ORCA.[82] First, the high-spin configuration was calculated, then the spin directions on two iron atoms in $[4Fe4S]_H$ and on Fe_p in $[2Fe]_H$ of the H-cluster were inverted, and finally the system was converged to the antiferromagnetic configuration. Transition energies and probabilities in the pre-K-edge absorption (c2v) and $Kß_{2,5}$ emission (v2c) regions were calculated for model or crystal structures as described.[50,60,64,65,83,84] For comparison with experimental spectra to the calculated c2v and v2c stick spectra Gaussian broadening was applied, and the amplitudes of the spectral envelopes were scaled, for the H-cluster models using the same factor for all c2v spectra (x270) and the same factor for all v2c spectra (x0.5). (The different scaling factors result from normalization of the experimental c2v spectra at the XANES edge jump of unity and the v2c spectra on the Kß line integral of unity using an eV energy axis.) Calculated c2v spectra include the 200 transitions (sticks) at lowest energies and calculated v2c spectra include all transitions (sticks) at energies higher than 7080 eV. The energy axes of calculated spectra in the c2v (~10 eV) and v2c (~40 eV) regions were multiplied (stretched) by the same empirical factor of 1.3,[64,65] and the resulting spectra were shifted on the energy axes by 181 eV, which facilitated comparison of experimental and calculated spectra on a common energy axis, as previously.[50,57,61,62] Notably, the energy shift corresponds to a systematic small underestimation of the energy differences between the 1s and valence levels by ~2.5% at 7100 eV. The stretching factor at the highest transition energies added maximally ~3 eV or ~0.05% (c2v) or ~10 eV or ~0.15% (v2c) to this figure, which we consider as being within the possible accuracy limitations of the DFT approach. As shown in Figure S5 for the *red* and *sred* states, the energy axes scaling, besides facilitating display on a common energy axis, did not affect the good agreement between experimental and calculated XAE spectra and, in particular, did not alter the shape of the respective spectral differences. Examples of ORCA input files are shown in Table S3.

RESULTS

Experimental Rationale for XAE on the H-Cluster of HydA1. Figure 2 summarizes the experimental strategy and theoretical foundations of our XAE experiments on the H-cluster.[60] The relevant X-ray absorption and emission spectra here are exemplified for apo-HydA1 protein containing only the $[4Fe4S]_H$ cluster[20] and for a synthetic diiron-adt complex with a similar structure as $[2Fe]_H$.[21,22,85] The pre-edge region of the K-edge absorption spectrum corresponds to core-to-valence (c2v) electronic excitation transitions (e.g., 1s → 3d). The $Kß_{2,5}$ region of the X-ray emission spectrum monitors valence-to-core (v2c) radiative electronic decay (e.g., 3d → 1s). Collection of Kß emission (e.g., v2c) spectra using nonresonant excitation at energies far above the iron K-edge (7600 eV) or of c2v spectra using total fluorescence (Kα) emission detection yields spectra representing the stoichiometric sum of the individual contributions of all six iron atoms in the H-cluster.[66] Site-selective detection of c2v spectra is established due to the spin-polarization of the Kß emission, which splits the line into the Kß′ and $Kß_{1,3}$ features.[47,57−59] The Kß′ emission is enhanced for increasing numbers of unpaired 3d electrons, i.e., in high-spin vs low-spin iron,[47,54,58,60] and for the H-cluster, the $Kß_{1,3}$ and Kß′ spectral differences of the $[4Fe4S]_H$ and $[2Fe]_H$ units

dx.doi.org/10.1021/ic502047q | Inorg. Chem. 2014, 53, 12164−12177

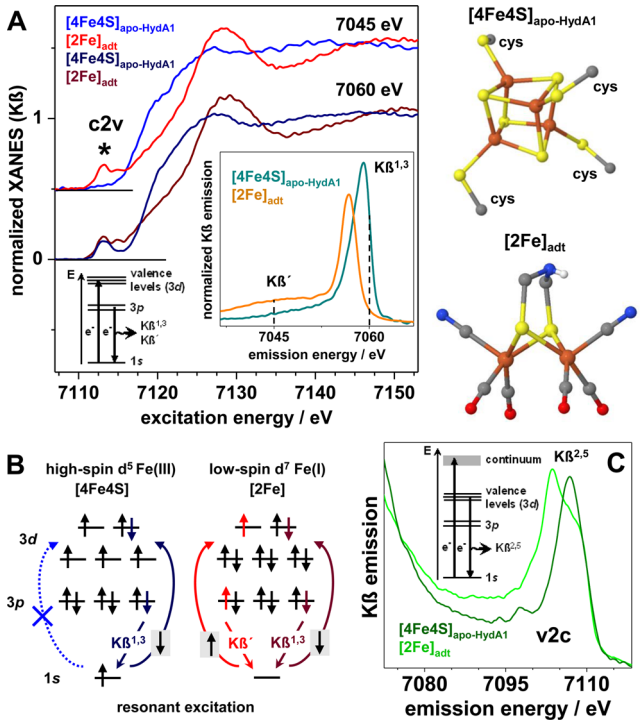

Figure 2. Spin- and site-selective X-ray spectroscopy. (A) left: Kß-detected K-edge spectra of apo-HydA1 protein binding only the [4Fe4S] unit[20] of the H-cluster and of a synthetic [2Fe] model complex[85] (5 mM aqueous solution) with a bridging adt ligand similar to the diiron site in the H-cluster. The Fe pre-edge absorption (core-to-valence excitation, asterisk) for $Kß_{1,3}$ emission detection (7060 eV) selectively probes the high-spin iron in the [4Fe4S] complex and for Kß′ emission detection (7045 eV) probes the low-spin iron in the [2Fe] complex. This rationale holds true also for the two subcomplexes of the H-cluster.[60] The inset shows the Kß emission spectra for resonant excitation (7113.5 eV); dashed lines mark the two detection energies. Right: crystal structures of the iron complexes[20,85] (S, yellow; N, blue; O, red; C, gray; H, white; Fe, orange; cys = cysteine). Relevant electronic excitation and decay processes are shown in atomic level diagrams. (B) Simplified atomic-level schemes for electronic excitation and decay leading to the Kß emission features. Kß′ emission results from interactions between unpaired metal 3d spins and the decaying 3p electron with the same spin flavor. For resonant excitation, for high-spin iron, i.e., Fe(III) in $[4Fe4S]_H$, excitation of an α-spin 1s electron does not occur, and 3p electrons cannot interact with unpaired 3d spins, which explains the absence of the pre-edge absorption feature for Kß′ detection, whereas for low-spin iron, i.e., formal Fe(I) in $[2Fe]_H$, excitation of α- and ß-spin 1s electrons is feasible and 3p electrons interact with unpaired 3d spins so that Kß′ and $Kß_{1,3}$ lines are observed. (C) $Kß_{2,5}$ emission lines (valence-to-core decay) for nonresonant excitation (7600 eV). In the case of the H-cluster, both subcomplexes contribute stoichiometrically to the $Kß_{2,5}$ emission. The model spectra and our previous studies[60] reveal that $[4Fe4S]_H$ contributes mainly at higher energies, whereas $[2Fe]_H$, due to its CO and CN^- ligands,[50,60,64,65] contributes also at lower energies, which establishes sensitivity to CO coordination and redox changes in the H-cluster.

are further enhanced by the varying oxidation states and coordination environments of their iron atoms (Figure 1).[50,60,65] For resonant excitation in the pre-edge absorption region and Kß′ detection, predominantly the low-spin iron centers (i.e., in $[2Fe]_H$) contribute to the c2v spectrum, whereas for detection at high $Kß_{1,3}$ energies the high-spin iron centers (i.e., in $[4Fe4S]_H$) dominate (Figure 2). This facilitated detection of individual c2v spectra of the $[4Fe4S]_H$ or $[2Fe]_H$ units of the H-cluster.[60]

Oxidation State of Iron in the HydA1 Samples. Redox changes of iron in the H-cluster, which were expected to occur in response to the oxidative or reductive treatments of HydA1, were verified by energy shifts of total-fluorescence (Kα)-detected Fe K-edge absorption and nonresonantly excited Kß emission line spectra (Figure 3). The K-edge spectra revealed

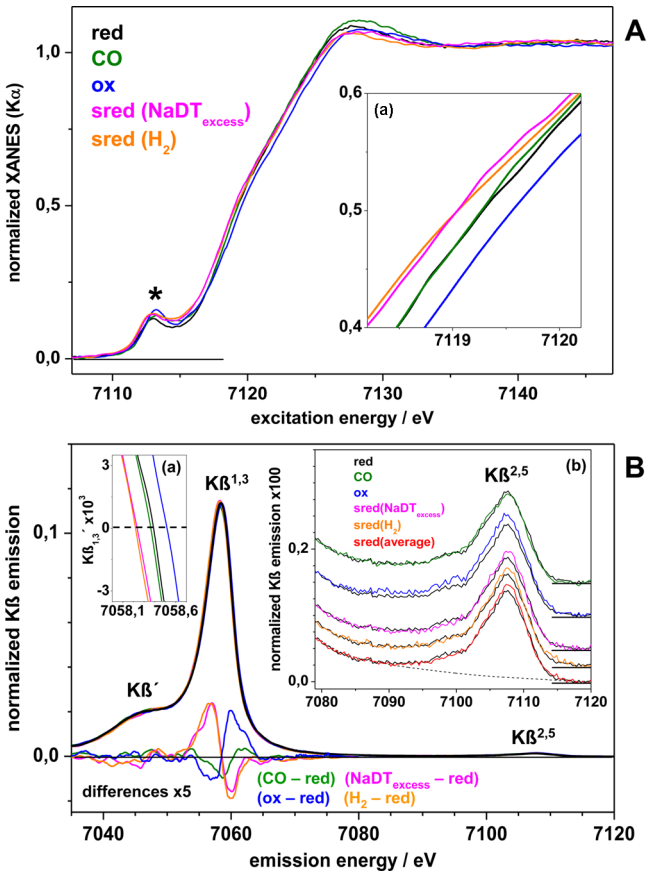

Figure 3. Redox changes at the H-cluster. (A) Total X-ray fluorescence (Kα)-detected Fe K-edge absorption spectra of the indicated HydA1 samples. The asterisk marks the pre-edge absorption. Inset: edge spectra around half-height in magnification showing energy shifts. (B) Fe Kß emission spectra for nonresonant excitation (7600 eV) and respective spectral differences in the Kß′ and $Kß_{1,3}$ regions. Inset (a): Zero-crossing region of the 1st derivatives of the $Kß_{1,3}$ spectra showing energy shifts. Inset (b): $Kß_{2,5}$ lines in magnification (vertically displaced for comparison); subtraction of the shown baseline (dashes) yielded the v2c spectra shown in Figures 5 and 9 (see also Figure S3).

edge energies for *red* and *CO* of ~7119.2 eV and ~0.25 eV shifts to higher (*ox*) or lower (*sred*) energies. The spectra of $NaDT_{excess}$ and H_2 reduced samples were similar, which suggested predominance of the same H-cluster state in the proteins (Figure 3A). Respective spectra therefore were averaged and denoted *sred* further on. Literature data of enzymes containing at most iron–sulfur clusters show K-edge shifts of ~2 eV per one-e^- oxidation or reduction per Fe ion.[60,66,86–89] The edge shift magnitudes for our HydA1 samples thus suggested the oxidation in *ox* or reduction in *sred* of ~0.75 of the six iron atoms in the H-cluster compared to *red*. Kß emission spectra using nonresonant excitation (7600 eV)

dx.doi.org/10.1021/ic502047q | Inorg. Chem. 2014, 53, 12164–12177

were collected for the HydA1 samples (Figure 3B). The overall spectral shape in the $K\beta_{1,3}$ and $K\beta'$ regions was similar in all samples. This suggested similar relative proportions of low- and high-spin iron atoms and overall similar degrees of metal−ligand bond covalency[90] in the studied H-cluster states. The $K\beta_{1,3}$ energies for *red* and *CO* were similar, but a ∼0.1 eV energy upshift in *ox* or energy down-shift in *sred* were observed (Figure 3B). For Fe(II)/Fe(III) conversion in FeS cluster dominated proteins or compounds showing only iron−sulfur bonds, $K\beta_{1,3}$ line shifts of ∼0.7 eV per Fe ion have been estimated.[60] The Kß emission thus suggested the oxidation in *ox* or reduction in *sred* of at least ∼0.8 Fe ions of the H-cluster compared to *red*. In summary, the absorption and emission data were consistent with the expected one-e^- oxidation in *ox* or one-e^- reduction in *sred* of the H-cluster relative to the *red* state in the majority of the HydA1 protein.[91] This facilitated detection of alterations in the XAE spectra of the different HydA1 samples as analyzed in the following.

XAE on the *ox*, *red*, and *CO* States of the H-Cluster. K-edge spectra of the HydA1 samples collected for Kß′- or $K\beta_{1,3}$-emission detection showed pronounced differences, which were attributable mainly to the varying contributions from the $[4Fe4S]_H$ and $[2Fe]_H$ units of the H-cluster.[60] In addition, spectral changes in response to the protein treatments were observed (Figure 4). However, the main K-edge shape changes were not expected to be straightforwardly indicative of relatively small geometry changes at the H-cluster and therefore were not analyzed further. The intensity planes in the energy regions of the pre-edge absorption and the $K\beta_{1,3}$ and Kß′ emission lines were collected for the HydA1 samples (Figure 4, inset), and pre-edge absorption spectra at high resolution were derived from the data. Background subtraction (Figure 4B) yielded the core-to-valence absorption (c2v) spectra of the *ox*, *red*, and *CO* samples shown in Figure 5.

The $K\beta_{1,3}$-detected c2v spectra resembled the spectrum of apo-HydA1 containing only the cubane cluster[20] and hence were assigned to $[4Fe4S]_H$.[60] They showed relatively minor shape and intensity variations among the H-cluster states, for example, overall increased intensity for *ox* compared to *red* (Figure 5A). The Kß′-detected c2v spectra differed strongly from the $K\beta_{1,3}$-detected spectra and were attributed to $[2Fe]_H$, as previously.[60] They revealed more prominent intensity and energy variations of the absorption peak features for the four HydA1 samples (Figure 5A), which were analyzed in the following using DFT calculations.

DFT calculations were carried out on model structures (Table S2) of the H-cluster in the *red*, *ox*, and *CO* states, yielding theoretical c2v spectra for $[4Fe4S]_H$ and $[2Fe]_H$ (Figure 5A). For *red*, only the calculated spectrum for a structure with an Fe−Fe bridging (CO) ligand at $[2Fe]_H$ and an open coordination site at Fe_d (Figure 6) reproduced the three main spectral maxima of the $[2Fe]_H$ spectrum (Figure 5A). The spectra calculated individually for Fe_p and Fe_d showed that the lowest-energy absorption peak was dominated by the square-pyramidal Fe_d (Figure 5A). $[2Fe]_H$ spectra for structures with an unoccupied bridging position and an apical (CO) at Fe_d or with a terminal hydride at Fe_d showed diminished intensities in the ∼7112 eV absorption region and peak energy shifts (Figure 6), which were in disagreement with the experimental data (Figure 5A). This favored a bridging (CO) ligand and seemingly excluded an iron-hydride bond in the *red* state of the H-cluster, in agreement with our previous results.[60] For *CO*, an additional terminal (CO) ligand at Fe_d in a

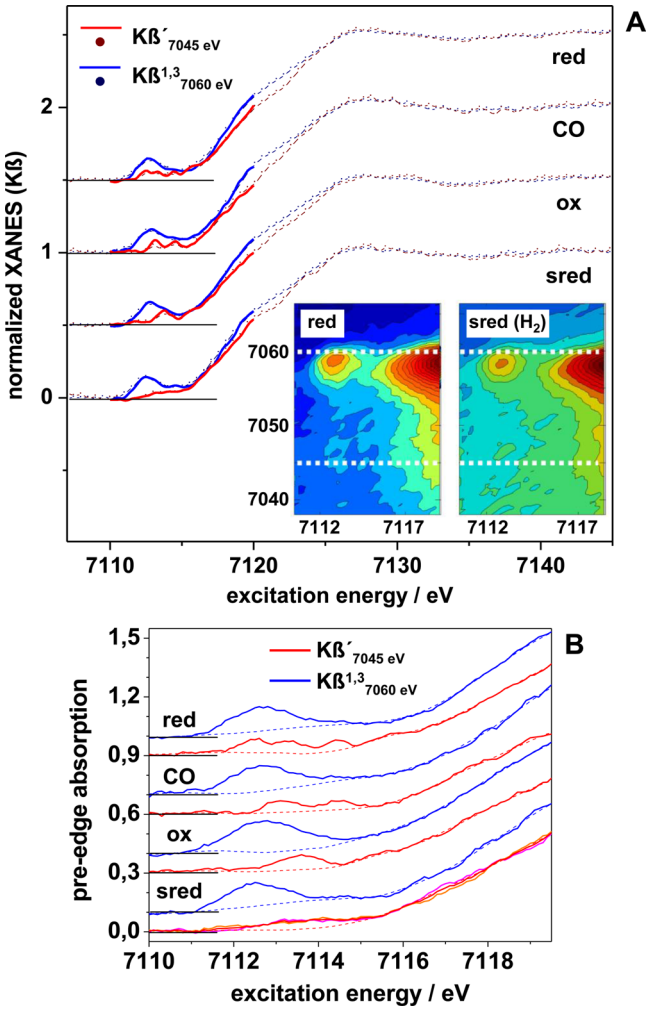

Figure 4. Kß-detected Fe K-edge spectra of the H-cluster. (A) K-edge spectra collected at indicated detection energies (dotted lines, shown at a resolution of 0.5 eV per data point) and pre-edge absorption spectra (solid lines, 0.1 eV per data point) derived from transects through absorption/emission plane data as shown in the inset. The spectrum denoted *sred* represents the average of spectra for $NaDT_{excess}$ and H_2 reduced HydA1. Spectra were vertically shifted for comparison. Inset: absorption/emission plane data for *red* and *sred* samples (dark red to dark blue, highest to lowest intensities; different colors in the two graphs correspond to different absolute emission intensities for the two samples). Pre-edge spectra were derived in the directions of the dashed lines for energy ranges of 7043.5−7046.5 eV and 7059.0−7061.0 eV and scaled to the amplitudes of the K-edge spectra. (B) Pre-edge spectra for HydA1 for $K\beta_{1,3}$ or Kß′ detection (vertically shifted for comparison) from (A) (solid lines) together with baseline curves (dashed lines), subtraction of which yielded the experimental c2v spectra in Figures 5 and 9. Magenta and orange lines show spectra for $NaDT_{excess}$- or H_2-reduced HydA1 in the *sred* state. For further c2v spectra of the *red* and *sred* states see Figure S4.

structure with the same redox state as *red* (Figure S1) already accounted for the spectral difference (*CO* − *red*) (Figure 5A). The calculated spectral difference including the c2v spectrum for a one-e^- more oxidized *CO* structure (*COox*) showed increased negative features around 7113 and 7115 eV (Figure S1), which was not observed in the experiment. A structure for *ox*, one-e^- more oxidized than *red* and containing a bridging (CO), reproduced the experimental c2v data well (Figure 5A).

Emission spectra in the Kß satellite lines region for nonresonant excitation (7600 eV) were collected for the

dx.doi.org/10.1021/ic502047q | *Inorg. Chem.* 2014, 53, 12164−12177

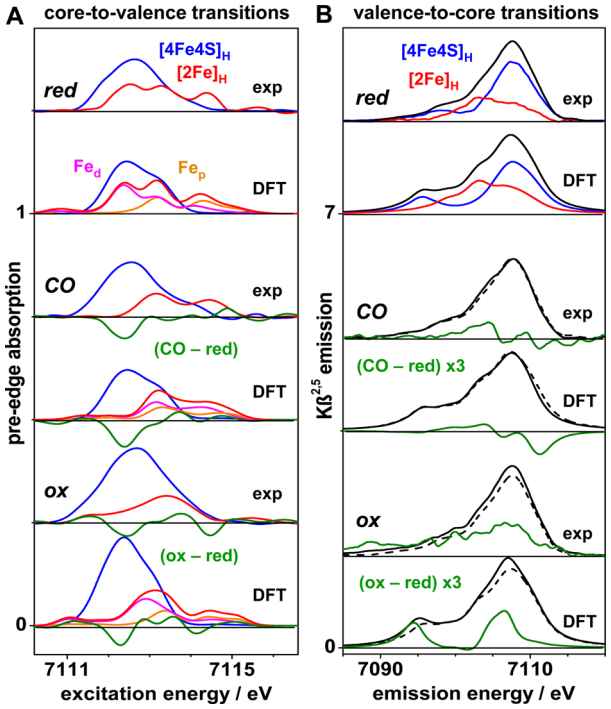

Figure 5. Core-to-valence (pre-edge) absorption and valence-to-core ($K\beta_{2,5}$) emission spectra of the reduced, oxidized, and (CO)-treated H-cluster. (A) Experimental (exp) c2v spectra from Fe K-edge data (Figure 4) for Kß detection at 7045 eV (red lines) or 7060 eV (blue lines) and spectral differences for $[2Fe]_H$ (green), compared to DFT-calculated spectra (Gaussian broadening 0.5 eV). (B) Experimental v2c spectra from Kß data (Figure 3B) for nonresonant excitation (dashes, *red*) and spectral differences (green) compared to DFT-calculated spectra (Gaussian broadening 3 eV). The v2c spectrum for $[4Fe4S]_H$ (blue line) was obtained on apo-HydA1, the $[2Fe]_H$ spectrum (red line) is the stoichiometric spectral difference (HydA1-*red* − apo-HydA1 x0.66). Calculated c2v and v2c spectra correspond to structures in Figure 11.

HydA1 samples, and extraction of the $K\beta_{2,5}$ line features (Figures 3B and S3) yielded the valence-to-core (v2c) spectra of the H-cluster shown in Figure 5. For *red*, the different spectral contributions from $[4Fe4S]_H$ and $[2Fe]_H$ to the sum spectrum were revealed by comparison to the spectrum of apo-HydA1.[60] Spectral changes between the states became discernible in the differences (*ox* − *red*) and (*CO* − *red*) (Figure 5B). The DFT-calculated v2c spectrum of the unprotonated *red* structure was more similar to the experimental *red* spectrum than the spectrum of a protonated structure in showing, e.g., lower intensity around 7108 eV (Figures 5B and 6), again suggesting the absence of an iron-hydride bond in *red*. The calculated spectral difference (*CO* − *red*) showed mostly negative intensities around 7110 eV, in agreement with the experimental data (Figure 5B). The calculated spectral difference including the *COox* structure, however, showed mostly positive features around 7110 eV (Figure S1), which was unlike the experiment. Notably, the HOMO was located at $[2Fe]_H$ and the LUMO at $[4Fe4S]_H$ in the *CO* model structure, whereas this was reversed in the *COox* structure (Figure S1). The calculated spectral difference including the c2v spectrum for the *ox* model structure with a bridging (CO) ligand reproduced the experimental c2v data well (Figure 5B). In summary, comparison of experimental and calculated v2c spectra revealed particularly good agreement for

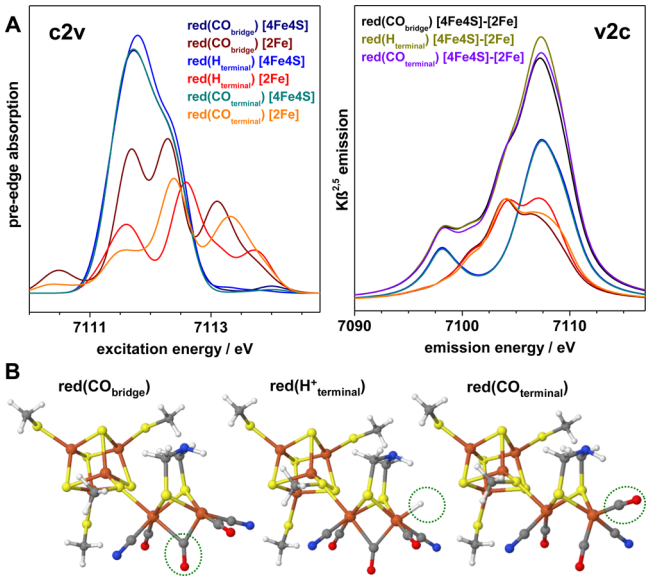

Figure 6. XAE spectra from DFT calculations for three model structures of *red*. (A) Left: calculated c2v spectra for the $[4Fe4S]_H$ and $[2Fe]_H$ subcomplexes in the structures in (B). Right: calculated v2c spectra for the whole H-cluster and the $[4Fe4S]_H$ and $[2Fe]_H$ subcomplexes (red and blue colors) for the structures in (B). (B) H-cluster model structures from DFT for the *red* state. Dotted circles mark the main structural differences of the models. Color code: gray, C; yellow, S; orange, Fe; blue, N; red, O; white, H.

the same model structures of *red*, *ox*, and *CO*, which accounted also for the c2v spectra, emphasizing the consistency and complementary character of the two data sets.

Detection of Iron-Hydride Bonds in Model Complexes. We investigated whether the formation of iron-hydride bonds was detectable by XAE in synthetic iron compounds, for which crystal structures were available (Table S1). The model complexes reveal the effects of exchanging a (CO) ligand against a terminal hydride in a low-spin monoiron complex ($\mathbf{1}_{FeCO}$, $\mathbf{1}_{FeH}$) or additional binding of a bridging hydride ($\mathbf{2}_{2Fe}$, $\mathbf{2}_{2Fe\mu H}$) or even of replacing two sulfur bridges by two μH bridges ($\mathbf{3}_{2Fe2\,\mu S}$, $\mathbf{3}_{2Fe2\,\mu H}$) in low- (**2**) or high- (**3**) spin diiron complexes. For these complexes, the Kα-detected K-edge absorption spectra and Kß emission line spectra showed pronounced shape and energy variations due to the varying iron spin state, ligation environment, and absence or presence of iron-hydride bonds (Figure 7). From the data in Figure 7, the experimental c2v or v2c spectra were extracted and are shown in Figure 8. Theoretical c2v and v2c spectra for the six complexes were calculated by DFT using the crystallographic coordinates (Table S1). The calculated spectra almost quantitatively reproduced the overall experimental spectral shape and energy changes and in particular accounted for the spectral differences due to terminal or bridging hydride binding (Figure 8). Notably, for $\mathbf{3}_{2Fe2\,\mu S}$ only antiferromagnetic coupling of the high-spin Fe(III) ions produced spectra in agreement with the experiment, emphasizing that XAE can provide specific information on the magnetic coupling mode of the iron atoms as determined by the spin orientation. We conclude that the used DFT approach facilitates quantitative calculation of c2v and v2c spectra for known iron-hydride structures, which we consider as compelling evidence that hydride binding to the H-cluster of HydA1 would be accessible as well.

dx.doi.org/10.1021/ic502047q | *Inorg. Chem.* 2014, 53, 12164−12177

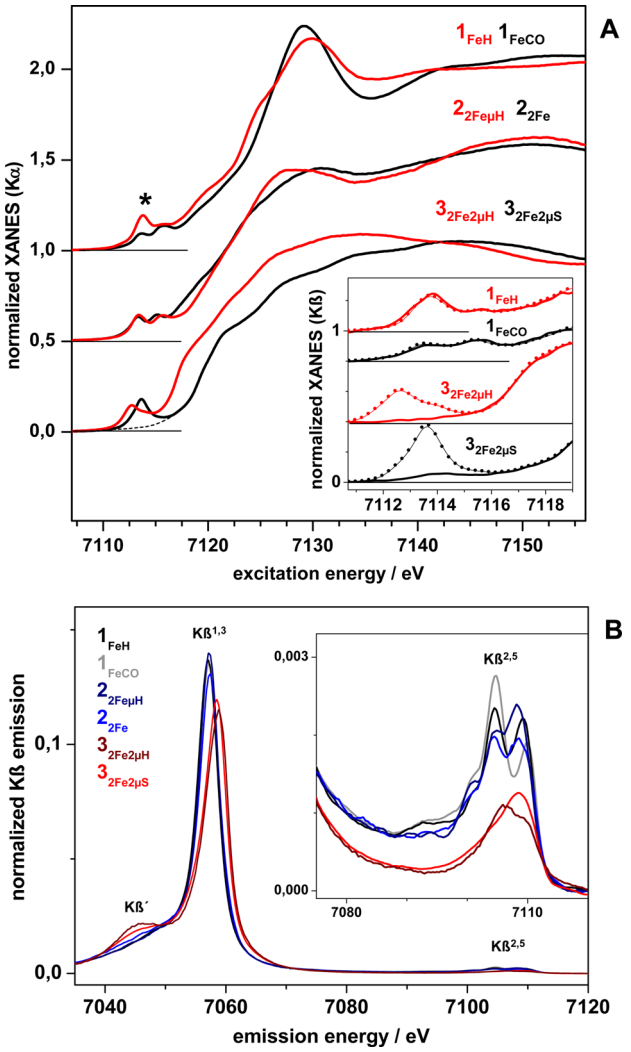

Figure 7. XAE spectra of synthetic iron complexes. Data are for powder samples; crystal structures are shown in Figure 8. (A) Kα-detected Fe K-edge spectra (vertically shifted for comparison). Subtraction of baseline curves (exemplified for $\mathbf{3}_{2Fe2\,\mu H}$ by the dashed line) in the pre-edge region (asterisk) yielded the c2v spectra in Figure 8. Inset: Kß-detected pre-edge absorption spectra of the indicated samples at Kß′ energies (7045 ± 1 eV, thick lines) or Kß$_{1,3}$ energies (dotted lines; $\mathbf{1}_{FeH}$ and $\mathbf{1}_{FeCO}$, 7056 ± 0.5 eV and $\mathbf{3}_{2Fe2\,\mu H}$ and $\mathbf{3}_{2Fe2\,\mu S}$, 7058 ± 0.5 eV); Kß′- and Kß$_{1,3}$-detected pre-edge spectra of $\mathbf{2}_{2Fe\mu H}$ and $\mathbf{2}_{2Fe}$ have been reported previously;[61] the small pre-edge absorption in the Kß′-detected spectrum of $\mathbf{3}_{2Fe2\,\mu S}$ may reflect a minor contribution from a lower spin state of the compound at the measuring temperature of 20 K. (B) Normalized Kß emission spectra for nonresonant excitation (7600 eV). Inset: Kß$_{2,5}$ emission spectra in magnification; baseline subtraction yielded the v2c spectra shown in Figure 8. Data points in (A) and (B) were connected by spline curves for display.

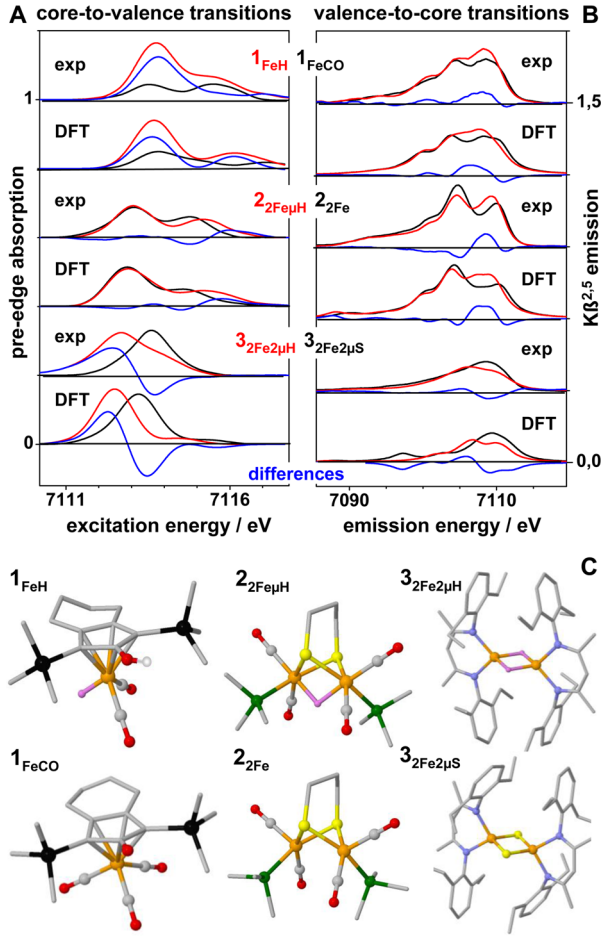

Figure 8. Iron-hydride bond detection in synthetic iron complexes. Experimental c2v (A) and v2c (B) spectra (derived from data in Figure 7) and spectral differences (blue lines) are compared to DFT-calculated spectra for the complexes in (C). Calculated c2v and v2c stick spectra were broadened by Gaussians (0.5 or 3 eV) and scaled to the experimental mean spectral areas for **1**, **2**, or **3**. Data points in (A) and (B) are connected by spline curves for display. (C) Crystal structures (coordinates in Table S1), most protons were omitted for clarity. Color code: orange, Fe; yellow, S; blue, N; red, O; green, P; black, Si; gray, C; white, H; magenta, hydride.

The site-selectivity for discrimination of low- or high-spin iron centers using narrow-band Kß emission detection at Kß′ or Kß$_{1,3}$ energies of X-ray absorption spectra could be affected by multiplet contributions spread over the hole Kß range from both iron species. The Kß-detected XANES spectra of the high-spin iron centers in the [4Fe4S] cluster in apo-HydA1 (Figure 2A) and in the diiron model compounds $\mathbf{3}_{2Fe2\,\mu S}$ and $\mathbf{3}_{2Fe2\,\mu H}$ (Figure 7A, inset) show that the pre-edge absorption (c2v) features are similar for Kα- or Kß$_{1,3}$ detection, but absent for Kß′ detection, due to the spin selectivity of the Kß′ emission. On the other hand, for the low-spin iron centers in the $[\mathbf{2Fe}]_{adt}$ model (Figure 2A), in the monoiron compounds $\mathbf{1}_{FeH}$ and $\mathbf{1}_{FeCO}$ (Figure 7A, inset), and in the diiron compounds $\mathbf{2}_{2Fe}$ and $\mathbf{2}_{2Fe\mu H}$,[61] the pre-edge absorption features are similar for Kα-, Kß$_{1,3}$, and Kß′ detection. We have previously shown that EXAFS spectra (from nonresonant X-ray excitation) of the H-cluster in HydA1 preferentially monitor the $[4Fe4S]_H$ subcluster for Kß′ (7045 eV) detection, but the $[2Fe]_H$ subcluster for detection at selected Kß$_{1,3}$ energies.[57] These findings suggest that multiplet contributions from high-spin iron for resonant excitation seem not to contribute significantly to the Kß′ emission region, which further corroborates that pre-edge spectra of low-spin iron centers can be obtained selectively using Kß′ detection both in model compounds and in HydA1.

Iron-Hydride Bond Formation in *sred*. The experimental c2v and v2c spectra of *sred* were derived from the respective Kß-detected K-edge absorption and Kß emission line data (Figures 3, 4, and S3) and are compared to the spectra of *red* in Figure 9. The site-selective c2v spectra of *sred* and *red* showed pronounced differences, in particular strongly diminished

dx.doi.org/10.1021/ic502047q | Inorg. Chem. 2014, 53, 12164−12177

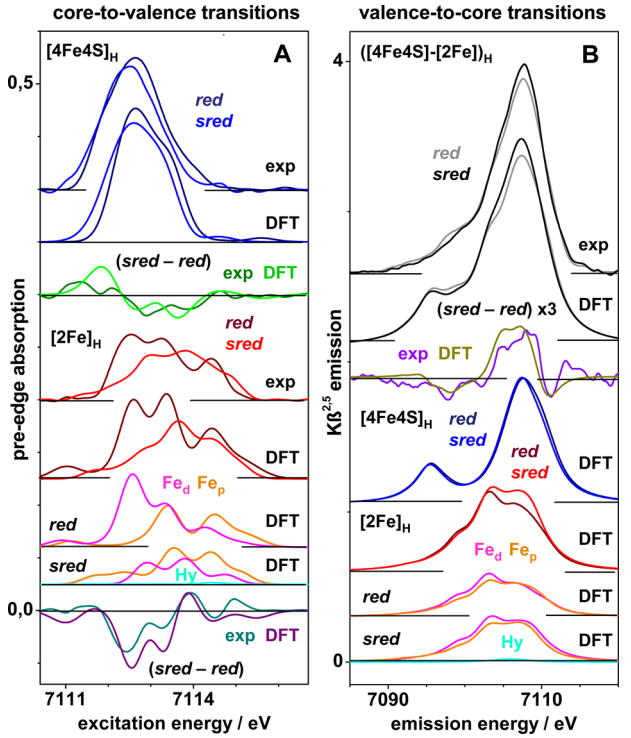

Figure 9. Hydride binding to the super-reduced H-cluster. Comparison of experimental (exp) c2v spectra (A) and v2c spectra (B) of *red* and *sred* HydA1 samples, difference spectra (*sred* − *red*), and DFT-calculated spectra for an unprotonated *red* structure and a one-e$^-$ more reduced *sred* structure with a bridging hydride (Figure 11). Spectra were derived as shown in Figures 3 and 4. Spectra denoted Hy (cyan) represent transitions into or from MOs with hydride character (Figure 11). For a second set of c2v and v2c spectra of *red* and *sred* and respective spectral differences, see Figure S4.

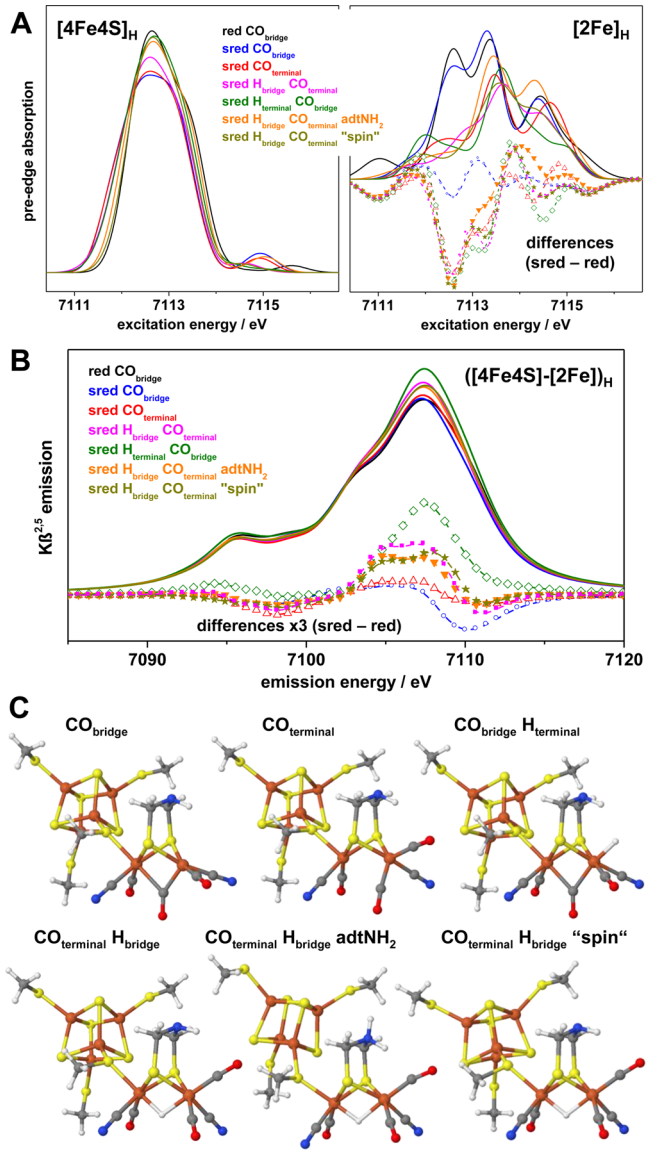

Figure 10. XAE spectra for *sred* model structures from DFT. (A) Calculated c2v spectra for *red* (Figure 11) and the *sred* structures in (C) for $[4Fe4S]_H$ (left) and $[2Fe]_H$ together with the difference spectra (*sred* − *red*) (right). (B) Calculated v2c spectra for the H-cluster for structures as in (A) together with the difference spectra (*sred* − *red*). (C) H-cluster model structures for *sred* (gray, C; yellow, S; orange, Fe; blue, N; red, O; white, H); the double-protonated adt nitrogen atom is denoted adtNH$_2$, "spin" denotes a structure with opposite α- and ß-spin orientations on the irons in $[4Fe4S]_H$ compared to *sred* (H_{bridge} $CO_{terminal}$). The structures are shown in slightly different orientations for clarity.

absorption at lowest energies and broadened transitions at higher energies for the $[2Fe]_H$ spectrum of *sred* (Figure 9A). These differences were observed for the NaDT$_{excess}$- and H$_2$-reduced *sred* samples. The v2c spectrum of *sred* revealed smaller amplitudes at low energies and a larger main maximum compared to *red* (Figure 9B). The v2c spectral differences between *red* and *sred* were relatively small, but exceeded the noise level of the data and were not significantly affected by the use of slightly different data processing procedures (see Figure S3 for details). Again, similar spectral changes were detected for the NaDT$_{excess}$- and H$_2$-reduced *sred* samples. Six structural models for *sred* were constructed, which were one-e$^-$ more reduced than *red* and comprised either a bridging (CO) ligand or a terminal (CO) at Fe$_d$ in $[2Fe]_H$ in protonated or unprotonated centers, an additional proton at the adt nitrogen, or different spin orientations (Figure 10).

Relatively minor differences in the calculated c2v spectra for $[4Fe4S]_H$ of the six *sred* structures were observed (Figure 10A). The experimental c2v spectrum of $[4Fe4S]_H$ therefore was not indicative of the *sred* configuration (Figure 9A). The calculated c2v spectra of $[2Fe]_H$ for *sred* and *red* with a bridging (CO) ligand were rather similar, for example, showing a pronounced low-energy maximum and thus unlike the experimental spectrum of *sred* (Figures 9A and 10A). This favored a terminal (CO) ligand at Fe$_d$ in *sred*. The c2v spectra for $[2Fe]_H$ in the other *sred* structures overall were quite alike (Figure 10A), meaning that rotation of the (CO) and the hydride between the bridging and terminal positions, as well as an additional proton at the adt nitrogen or an alternative spin configuration caused relatively small spectral changes. However, the main features of the experimental difference (*sred* − *red*) of $[2Fe]_H$, i.e., pronouncedly negative amplitudes around 7113 eV and negligible amplitudes at >7113.5 eV, were best reproduced by the calculated differences for the three *sred* structures with a terminal (CO) at Fe$_d$ and a μH, whereas a terminal hydride resulted in negative amplitudes around 7114 eV, which was not observed experimentally (Figures 9A and 10A). The calculations furthermore revealed that a μH species altered mostly the c2v spectrum of Fe$_d$. The increased symmetry at Fe$_d$ in the presence of the hydride, leading to altered contributions of

dx.doi.org/10.1021/ic502047q | *Inorg. Chem.* 2014, 53, 12164−12177

metal- and ligand-centered orbitals to the target MOs (not shown) and to diminished transition intensities and energy shifts, largely could explain the decreased amplitude of the lowest-energy peak in the c2v spectrum of $[2Fe]_H$ for *sred*.

Further evidence for an iron-hydride bond in *sred* came from the v2c spectra (Figure 9B). The main features of the experimental spectral difference (*sred* − *red*), showing pronouncedly positive amplitudes at ∼7107 eV and smaller negative amplitudes at ∼7098 eV and ∼7111 eV, were not reproduced by the calculated differences for the unprotonated $[2Fe]_H$ structures of *sred* (Figures 9B and 10B). The spectral difference for *sred* with a terminal hydride and a bridging (CO) showed a larger positive maximum at ∼7107 eV than observed experimentally and lacked negative features at lower and higher energies (Figure 10B). The spectral differences for the *sred* structures with a terminal (CO) at Fe_d and a μH, however, were in good agreement with all main experimental spectral features (Figures 9B, 10B, and S3). A second proton at the adt nitrogen or a different spin orientation caused relatively minor changes of the v2c spectra, although the distribution of the calculated HOMO and LUMO over the six iron atoms of the H-cluster showed discernible differences (Figure S2). Notably, the calculations also revealed that the experimental v2c emission for *sred* comprised only very small contributions of electronic decay from MOs centered at the bridging hydride (Figure 9B).

Both the c2v and, in particular, the v2c spectral differences of $[4Fe4S]_H$ and $[2Fe]_H$ between the *red* and *sred* states of HydA1 were relatively small and may still be affected by noise contributions. In the case of the v2c spectra, which amount to only about 1.5% of the emission intensity in the whole Kß region, also the normalization procedure may affect the spectral differences. Therefore, second set of spectra was measured for the [FeFe]-hydrogenase protein, which was obtained by functional reconstitution of apo-HydA1 with the synthetic $[2Fe]_{adt}$ complex (Figure 2), yielding active holo-HydA1 enzyme as previously described.[21,22] The resulting c2v and v2c spectra of the *red* and *sred* states (for H_2- or $NaDT_{excess}$-reduction) and in particular the respective (*sred* − *red*) spectral differences of the reconstituted protein were very similar to the spectra obtained for the native enzyme (Figure S4). Accordingly, the comparison of two independent spectra for the *red* state and of four independent sets of c2v and v2c spectra for the *sred* state from native or reconstituted HydA1 and for H_2- or $NaDT_{excess}$-reduction (Figures 4, 9, S3, and S4) provided further evidence that the assigned spectral differences between the *sred* and the *red* states are reproducible and thus significant. The good agreement between the experimental and calculated spectral differences both for the HydA1 samples and for the model compounds indicates that the used normalization procedures for the XAS and XES spectra are adequate.

Molecular and Electronic Parameters of the H-Cluster Models. The H-cluster structures providing the best agreement between experimental and calculated XAE spectra of HydA1 are compiled in Figure 11. Starting from *ox*, the Fe−Fe distances in $[4Fe4S]_H$ and $[2Fe]_H$ increased by ∼0.05 Å per one-e^- reduction in *red* and *sred* (Table 1). The calculated Fe−C(=O/N) and Fe−S bond lengths were in reasonable agreement with previous XAS studies on HydA1 protein.[42,60,66,92] The asymmetric bridging (CO) ligand showed a ∼0.2 Å shorter bond at Fe_p in *ox* and *red*, but at Fe_d in *CO*. The bridging hydride in *sred* showed a ∼0.1 Å shorter bond to Fe_p. Close to one total net spin on $[4Fe4S]_H$ accounted for the

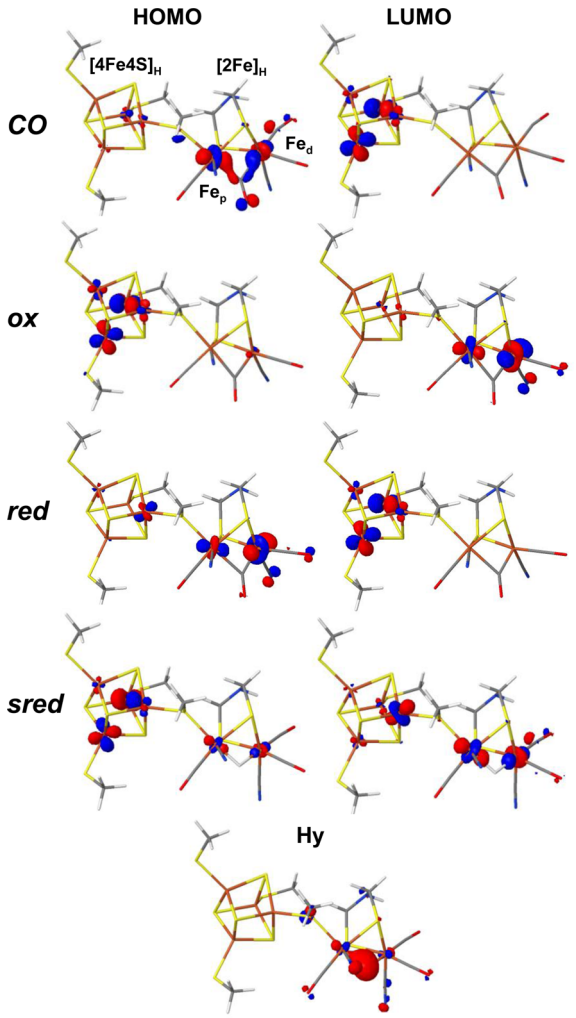

Figure 11. H-cluster model structures from DFT. The c2v and v2c spectra calculated for these structures were in best agreement with the experimental data. The *red* structure with a formal $Fe(II)_2Fe(III)_2Fe(I)_2$ oxidation state shows a bridging (CO) ligand at $[2Fe]_H$ and a vacant coordination site at Fe_d; the latter is occupied by an additional (CO) in the *CO* structure with the same oxidation state; the *ox* structure is one-e^- more oxidized and otherwise similar as *red*; the *sred* structure is one-e^- more reduced than *red*, Fe_d carries an apical (CO), and $[2Fe]_H$ holds a bridging hydride. HOMO and LUMO locations are indicated; Hy denotes an MO at the hydride, which contributes weakly to the XAE spectra of *sred*.

paramagnetic spin 1/2 states of *ox* and *sred*.[91] The LUMO was located at $[4Fe4S]_H$ and the HOMO, which was localized on $[2Fe]_H$, showed predominantly $Fe_d d(z^2)$ character in *red*, and was more evenly distributed over Fe_d and Fe_p in *CO*. However, the HOMO was located at $[4Fe4S]_H$ and the LUMO mostly at Fe_d in *ox* and more evenly distributed over Fe_p and Fe_d in *sred*. All calculated LUMO−HOMO energy differences were remarkably small (<0.25 eV) (Table 1). Notably, the calculated total energy of the *sred* structure with a μH and a terminal (CO) at Fe_d was ∼0.3 eV lower than the energy of the *sred* structure with a terminal hydride and a bridging (CO). However, differences in energy of comparable magnitude were observed for *sred* structures with, for example, different spin orientations.

Electronic transitions at lowest energies in the c2v spectra or at highest energies in the v2c spectra are dominated by dipolar

dx.doi.org/10.1021/ic502047q | Inorg. Chem. 2014, 53, 12164−12177

Table 1. Parameters of H-Cluster Models from DFT

H-cluster structure[a]	*ox*	*red*	*sred*	*CO*
Fe−Fe distance in $[4Fe4S]_H$, $[2Fe]_H$ [Å]	2.64, 2.55	2.69, 2.60	2.70, 2.66	2.69, 2.87
mean Fe−C(O/N), Fe−S distance in $[2Fe]_H$ [Å]	1.86, 2.33	1.86, 2.36	1.81, 2.33	1.87, 2.40
Fe-μ(CO) or Fe-μ(H) distance at Fe_p, Fe_d [Å]	2.02, 1.88	2.12, 1.81	1.63, 1.74	1.87, 2.15
spin on iron $[4Fe4S]_H$, $[2Fe]_H$	1.72, −0.93	0.11, 0.15	0.56, 0.22	0.20, 0.17
Fe_p, Fe_d	−0.16, −0.77	0.04, 0.11	0.13, 0.09	0.09, 0.08
number of occupied Fe*d* MOs[b] for Fe_p, Fe_d	7, 7	6, 8	7, 8	7, 7
ΔE (1s → 3d-3d → 1s) exp, DFT[c] [eV]	1.4, 1.5	1.6, 1.6	2.1, 2.4	1.9, 2.2
ΔE (LUMO-HOMO)[d] [eV]	0.13	0.22	0.03	0.21

[a]Data are for structures in Figure 11. [b]Values refer to the 10 lowest-energy MOs with main Fe*d* character. [c]Energy differences (ΔE) were derived from apparent 1s → 3d and 3d → 1s transition energies determined from c2v or v2c spectra as shown in Figure 12. [c,d]Calculated ΔE values were multiplied by a factor of 1.3[60] for comparison with experimental data.

transitions, that is, excitation into or decay from MOs with predominant Fe*d* character.[50,60,64,65] The respective apparent 1s → 3d or 3d → 1s energies were estimated from the experimental and calculated c2v or v2c spectra of the H-cluster (Figure 12 and Figures S6 and S7; see the legends). (We note that the term 3*d* here is used for convenience and encompasses

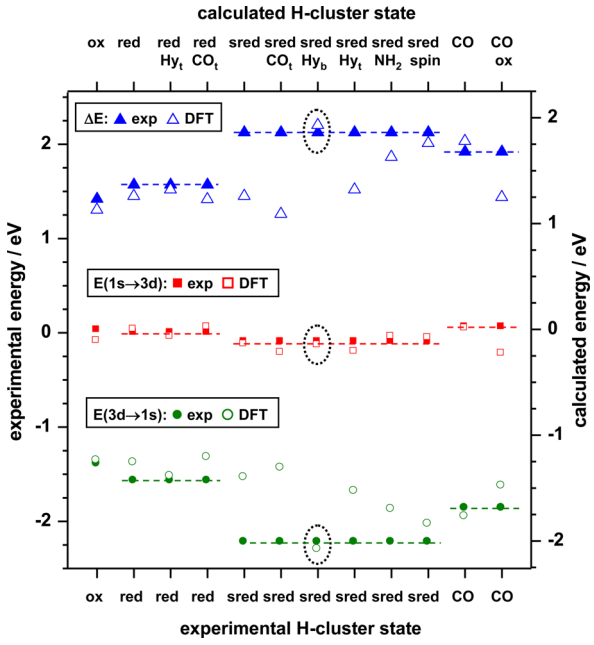

Figure 12. Electronic transitions from and into MOs with Fe*d* character. Experimental apparent transition energies represent the HydA1 samples and correspond to the lowest-energy inflection points (1s → 3d) in the Kα-detected pre-edge absorption spectra (Figure 3A) or to the highest-energy inflection points (3d → 1s) in the K$\beta_{2,5}$ emission spectra (Figure 3B, inset). The calculated apparent transition energies denote the respective low- or high-energy inflection points in the theoretical pre-edge absorption or K$\beta_{2,5}$ emission spectra for the whole H-cluster. Inflection point energies were determined as the zero-crossing point in the second derivatives of spectra as outlined in Figures S6 and S7. Values of 7112.07 or 7111.29 eV were subtracted from all experimental or calculated energies so that E(1s → 3d) for *red* (calculated data for the unprotonated structure with a bridging (CO) in Figure 11) was set to zero in both cases. The energy difference is defined as $\Delta E = E(1s \rightarrow 3d) - E(3d \rightarrow 1s)$. Dashed lines connect data points for the same experimental H-cluster states. Calculated H-cluster states correspond to structures in Figures 6, 10, 11, and S1 (Hy_t, terminal hydride at Fe_d; Hy_b, bridging hydride; CO_t, terminal (CO) at Fe_d; NH_2, double-protonated adt; spin, alternative spin state). Dotted circles mark values for the *sred* structure with a bridging hydride.

also minor ligand orbital contributions to the valence levels.) The experimental and calculated energies, as well as the respective energy differences (ΔE) between excitation and decay transitions, for our four favored DFT structures (Figure 11) were in particularly good agreement (Table 1, Figure 12). Larger deviations were observed for example for a *red* structure with a terminal (CO) ligand (Figure 6) or for the more oxidized *CO* structure (Figure S1). For *sred*, only for the structures with a bridging hydride (for both spin orientations) and in particular for the structure with a singly protonated N-adt nitrogen base (Figure 11) a ΔE value was calculated, which reproduced the ∼0.6 eV larger experimental energy difference for *sred* compared to *red* (Figure 12).

DISCUSSION

Site-selective discrimination of the high-spin iron in $[4Fe4S]_H$ and low-spin iron centers in $[2Fe]_H$ and complementary analysis of the whole H-cluster has provided novel X-ray spectroscopic fingerprints for the active site in algal [FeFe]-hydrogenase. This has facilitated assignment of specific model structures for the oxidized, reduced, super-reduced, and carbon monoxide-treated states of the H-cluster. For *CO*, binding of a surplus (CO)-ligand at Fe_d produced two near-octahedral iron atoms in $[2Fe]_H$, as in a crystal structure of (CO)-treated [FeFe]-hydrogenase.[93] In our *CO* samples, the major species presumably showed a formal $[4Fe4S]_H^{2+}Fe_p(I)Fe_d(I)$ oxidation state.[91] Anaerobic chemical oxidation of *red* yielded *ox* with a vacant site at Fe_d and likely a bridging (CO) ligand. Significant spin on Fe_d accounted for a paramagnetic mixed-valence $Fe_p(I)Fe_d(II)$ state,[91] but the net spin on $[4Fe4S]_H^{2+}$ and more symmetric occupancy of Fe*d*-dominated MOs of the two irons in $[2Fe]_H$ implied altered spin states in *ox* and *red*. Our XAE analysis and previous studies by other methods[36,37,91] thus converge toward similar structural models for the (CO)-inhibited and oxidized H-cluster.

Metal-hydride species are crucial in H_2 catalysis but are difficult to detect.[94] Our studies on crystallized model complexes clearly revealed the sensitivity of XAE for detection of electronic changes due to iron-hydride bond formation.[64,65] For the H-cluster, detection of pre-edge (c2v) spectra at two Kβ emission energies allowed for spectral discrimination of the different iron sites in the $[4Fe4S]_H$ and $[2Fe]_H$ units. It has been shown that charge transfer transitions (metal−ligand, d−d) can affect the spectral shape of the pre-edge absorption for narrow-band emission detection,[95,96] which may reduce the site-selectivity. Furthermore, multiplet contributions spread over the Kβ emission region may also affect the site-selectivity of pre-edge absorption spectra. Our analysis of several high- or

dx.doi.org/10.1021/ic502047q | *Inorg. Chem.* 2014, 53, 12164−12177

low-spin iron compounds has shown that for resonant excitation, multiplet contributions of high-spin iron to the Kß′ emission region seem to be negligible. The pronounced spectral differences in the pre-edges detected at Kß′ and $Kß_{1,3}$ energies and the good agreement between the experimental and calculated spectra for the individual Fe sites suggest that possible charge transfer or multiplet contributions to the spectra did not diminish the site-selectivity significantly and/or were small and not resolved experimentally both for the H-cluster and the model complexes.

For the nonparamagnetic *red* state of the H-cluster, it is debated whether $[2Fe]_H$ comprises an iron-hydride bond.[36,37,97,98] Our data suggest a bridging (CO) ligand at $[2Fe]_H$, which likely excludes a bridging hydride, and favors a vacant site at Fe_d in a formal $[4Fe4S]^{2+}Fe_p(I)Fe_d(I)$ state with asymmetric Fe*d* level degeneracy at the irons of $[2Fe]_H$ in *red*,[60] which lacks iron-hydride bonds. The fully reduced (*sred*) H-cluster in HydA1 has been characterized by infrared and magnetic resonance techniques,[36,37] but the presence of iron-hydride bonds has remained an open question. We show that *sred* structures with a bridging or terminal (CO) ligand and vacant coordination site(s) are not well in agreement with the XAE data. Instead, the data favors a terminal (CO) ligand at Fe_d, which is supported by infrared spectroscopy results.[36] This seemingly excludes a terminal hydride at Fe_d. Notably, H-cluster structures with a six-coordinated Fe_d carrying two (CO) ligands, one (CN^-), and a hydride and having initially an open bridging position at $[2Fe]_H$ in our hands were unstable in geometry optimization by DFT and converged toward configurations with either a bridging (CO) or a bridging hydride, depending on the starting structure. Structures with an open bridge might be stabilized by protein−cofactor interactions. At present, we consider such an option as less likely because the rotational freedom for $[2Fe]_H$ may be restricted due to space limitations, i.e., as seen in the crystal structures of bacterial [FeFe]-hydrogenases, and due to hydrogen-bonding to the CN^- ligands and the adt-nitrogen. A model structure for *sred* comprising a hydride bound slightly asymmetrically in the Fe−Fe bridging position at $[2Fe]_H$ provided the best agreement between calculated and experimental data sets of the complementary c2v and v2c spectra. We therefore suggest that *sred* as observed here contains a bridging hydride.

Our results and previous investigations[36,37] suggest that three main states of the H-cluster, namely, *ox*, *red*, and *sred*, predominantly accumulate under in vitro conditions in HydA1 (Figure 13). A key result of this study is that only in *sred*, an iron-hydride bond likely is formed at $[2Fe]_H$. In synthetic diiron model complexes for $[2Fe]_H$, μH species usually represent rather unreactive low-energy traps.[10,71] DFT studies have shown that reduced H-cluster structures with a μH are by ∼40 kJ $mmol^{-1}$ lower in energy than structures with a terminal hydride at Fe_d and (CO) ligand rotations exhibit considerable energetic barriers.[45,99] In a recent DFT study, a reaction path for H_2 formation was suggested, which exclusively involves terminally bound hydrogen species, as favored by energy-lowering effects of the amino acid environment of the H-cluster.[45] However, the proposed path accordingly involved only H-cluster species with a bridging (CO) at $[2Fe]_H$, which seems not to be supported by infrared data.[36,37] Imaginably, the influence of the amino acid environment, as well as the intrinsically asymmetric cysteine and (CO) ligation and effective oxidation state at the two irons of $[2Fe]_H$ may also

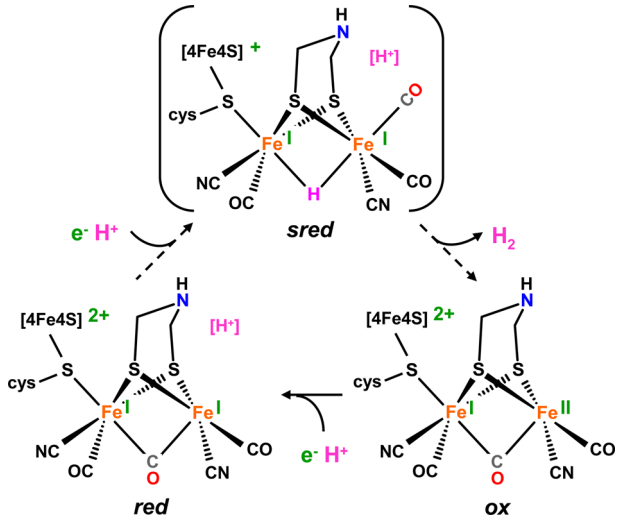

Figure 13. Tentative catalytic cycle of H_2 formation in [FeFe]-hydrogenase. The three shown intermediates accumulate in vitro in HydA1 under reducing or oxidizing conditions. Their structures and in particular the bridging hydride in *sred* were suggested by our XAE data. Dashed arrows and parentheses around *sred* symbolize the possible formation of additional transient states on the way to H_2 formation (cys = cysteine). Indicated redox states follow previous assignments.[36] Our DFT results may suggest more asymmetric Fe*d* level configurations for Fe_p and Fe_d in $[2Fe]_H$ in *red* and *sred* (Table 1).[60] [H+] denotes protonation events at presently unknown positions other than iron.

enhance the reactivity of H-cluster states with a bridging hydride. The pendant nitrogen base of the adt ligand likely plays a crucial role in proton management at the active site.[21,22,100] During the *ox* → *red* one-e^- reduction, electroneutral protonation of amino acids or thiol groups in a hydrogen-bonded network with the adt could keep the redox potential of the H-cluster constant,[101] facilitating the *red* → *sred* one-e^- reduction at a similar potential by the natural redox partner of HydA1, the ferredoxin PetF.[102] The *red* → *sred* transition then may be initiated by Fe−Fe bond protonation and H−H bond formation at the bridging hydride would be one option (Figure 13). However, the compatibility of the superior H_2 turnover rates of [FeFe]-hydrogenases[14] with pronounced structural changes at the H-cluster during the *red* → *sred* transition remains to be clarified.

The HOMO and LUMO energies are related to the first oxidation and reduction potentials of diiron model complexes, which exhibit large (2−3 eV) respective LUMO−HOMO energy gaps.[50,64,65] About 10-times smaller gaps for the studied H-cluster states in HydA1 were suggested by our XAE results and the DFT calculations. Apparently, such small energy gaps are achieved by coupling of the cubane cluster to $[2Fe]_H$,[60] leading to separation of the HOMO and LUMO on $[4Fe4S]_H$ or the diiron site. Presumably, this is a prerequisite for thermodynamically reversible redox reactions at negligible overpotentials in the [FeFe]-hydrogenases.[103] The actual H-cluster intermediate accumulating under steady-state conditions seemingly depends, e.g., on the presence (bacterial enzymes) or absence (HydA1) of relay iron−sulfur clusters.[36,91] For HydA1, we and others[36,37] have observed formation of the same *sred* species for proton reduction with external electron donor or under H_2 cleavage conditions without external acceptor in protein solutions. This is straightforwardly explained if *sred* is involved in the catalytic cycle in both H_2 formation and

dx.doi.org/10.1021/ic502047q | Inorg. Chem. 2014, 53, 12164−12177

cleavage directions. However, also slow and reversible formation at low potentials of a H-cluster species that is inactive in proton reduction but still able to oxidize H_2 has been deduced from electrochemical experiments on immobilized HydA1 enzyme, which was interpreted as placing *sred* on a reaction sidepath.[104] On the basis of our present and previous results,[36] we currently favor the interpretation that *sred* is an intermediate in the catalytic cycle. The occurrence, depending on conditions, of additional transient intermediates, however, cannot be excluded. In conclusion, we suggest a reaction scheme of the H-cluster involving at least two proton and electron transfer steps prior to the H_2 formation chemistry (Figure 13).

■ ASSOCIATED CONTENT

Supporting Information

Crystallographic coordinates of synthetic iron complexes (Table S1), coordinates of H-cluster model structures from DFT (Table S2), examples of ORCA input files (Table S3), XAE spectra for two DFT structures of (CO)-treated HydA1 (Figure S1), HOMO and LUMO configurations in three *sred* model structures with a bridging hydride (Figure S2), comparison of v2c spectra of *red* and *sred* (Figure S3), c2v and v2c spectra of apo-HydA1 reconstituted with $[2Fe]_{adt}$ (Figure S4), XAE spectra on two DFT-calculated energy axes (Figure S5), transition energy determination from experimental XAE spectra (Figure S6), transition energy determination from DFT-calculated XAE spectra (Figure S7). This material is available free of charge via the Internet at http://pubs.acs.org.

■ AUTHOR INFORMATION

Corresponding Author

*Phone: +49 30 838 56101. Fax: +49 30 838 56299. E-mail: michael.haumann@fu-berlin.de.

Present Addresses

[‖]Molecular Biotechnology, RWTH Aachen, 52074 Aachen, Germany.

[○]MAX IV Laboratory, Lund University, 22100 Lund, Sweden.

Author Contributions

[▽]P.C. and C.L. contributed equally to this work.

Notes

The authors declare no competing financial interest.

■ ACKNOWLEDGMENTS

M.H. thanks the Deutsche Forschungsgemeinschaft for a Heisenberg Fellowship and for funding (Grants Ha3265/3-1, Ha3265/6-1), the Bundesministerium für Bildung und Forschung for Grant 05K14KE1 within the Röntgen-Angström Cluster, and the ESRF for a Long Term Project. T.H. thanks the Deutsche Forschungsgemeinschaft (grant Ha2555/2-1) and the Volkswagen Foundation (grant "Biomimetic assembly of a photocatalytic unit for hydrogen production") for funding. P.C. thanks H. Dau (FU-Berlin) for constant support. We are grateful to M. Darensbourg (Texas A&M University) for kind support and valuable discussion. M.D. and Ch.L. were supported within the "Unicat" Cluster of Excellence Berlin. We thank P. Glatzel and J.-D. Cafun at ID26 of ESRF for excellent technical support and K. Klein (Ruhr-Universität Bochum) for generously providing the $[2Fe]_{adt}$ complex.

■ ABBREVIATIONS:

adt, azadithiolate; c2v, core-to-valence transitions; DFT, density functional theory; HOMO, highest (energy) occupied MO; HydA1, [FeFe]-hydrogenase from green algae; LUMO, lowest (energy) unoccupied MO; MO, molecular orbital; v2c, valence-to-core transitions; NaDT, sodium dithionite; XAE, combined XAS and XES spectroscopy; XAS, X-ray absorption spectroscopy; XES, X-ray emission spectroscopy

■ REFERENCES

(1) Rifkin, J. *The Hydrogen Economy*; Tarcher: London, 2002.
(2) Le Goff, A.; Artero, V.; Jousselme, B.; Tran, P. D.; Guillet, N.; Metaye, R.; Fihri, A.; Palacin, S.; Fontecave, M. *Science* **2009**, *326*, 1384−1387.
(3) Vignais, P. M.; Billoud, B. *Chem. Rev.* **2007**, *107*, 4206−4272.
(4) Mulder, D. W.; Shepard, E. M.; Meuser, J. E.; Joshi, N.; King, P. W.; Posewitz, M. C.; Broderick, J. B.; Peters, J. W. *Structure* **2011**, *19*, 1038−1052.
(5) Simmons, T. R.; Berggren, G.; Bacchia, M.; Fontecave, M.; Artero, V. *Coord. Chem. Rev.* **2014**, *270*−*271*, 127−150.
(6) Rauchfuss, T. B. *Science* **2007**, *316*, 553−554.
(7) Darensbourg, M. Y.; Bethel, R. D. *Nat. Chem.* **2012**, *4*, 11−13.
(8) Tard, C.; Pickett, C. J. *Chem. Rev.* **2009**, *109*, 2245−2274.
(9) Kruse, O.; Hankamer, B. *Curr. Opin. Biotechnol.* **2010**, *21*, 238−243.
(10) Gloaguen, F.; Rauchfuss, T. B. *Chem. Soc. Rev.* **2009**, *38*, 100−108.
(11) Besora, M.; Lledos, A.; Maseras, F. *Chem. Soc. Rev.* **2009**, *38*, 957−966.
(12) Nagel, Z. D.; Klinman, J. P. *Chem. Rev.* **2006**, *106*, 3095−3118.
(13) McGrady, G. S.; Guilera, G. *Chem. Soc. Rev.* **2003**, *32*, 383−392.
(14) Stripp, S. T.; Happe, T. *Dalton Trans.* **2009**, 9960−9969.
(15) Fontecilla-Camps, J. C.; Volbeda, A.; Cavazza, C.; Nicolet, Y. *Chem. Rev.* **2007**, *107*, 4273−4303.
(16) Peters, J. W.; Lanzilotta, W. N.; Lemon, B. J.; Seefeldt, L. C. *Science* **1998**, *282*, 1853−1858.
(17) Nicolet, Y.; Piras, C.; Legrand, P.; Hatchikian, C. E.; Fontecilla-Camps, J. C. *Structure* **1999**, *7*, 13−23.
(18) Pierik, A. J.; Roseboom, W.; Happe, R. P.; Bagley, K. A.; Albracht, S. P. *J. Biol. Chem.* **1999**, *274*, 3331−3337.
(19) Silakov, A.; Wenk, B.; Reijerse, E.; Lubitz, W. *Phys. Chem. Chem. Phys.* **2009**, *11*, 6592−6599.
(20) Mulder, D. W.; Boyd, E. S.; Sarma, R.; Lange, R. K.; Endrizzi, J. A.; Broderick, J. B.; Peters, J. W. *Nature* **2010**, *465*, 248−251.
(21) Esselborn, J.; Lambertz, C.; Adamska-Venkatesh, A.; Simmons, T.; Berggren, G.; Noth, J.; Siebel, J.; Hemschemeier, A.; Artero, V.; Reijerse, E.; Fontecave, M.; Lubitz, W.; Happe, T. *Nat. Chem. Biol.* **2013**, *9*, 607−609.
(22) Berggren, G.; Adamska, A.; Lambertz, C.; Simmons, T. R.; Esselborn, J.; Atta, M.; Gambarelli, S.; Mouesca, J. M.; Reijerse, E.; Lubitz, W.; Happe, T.; Artero, V.; Fontecave, M. *Nature* **2013**, *499*, 66−69.
(23) Posewitz, M. C.; King, P. W.; Smolinski, S. L.; Zhang, L.; Seibert, M.; Ghirardi, M. L. *J. Biol. Chem.* **2004**, *279*, 25711−25720.
(24) Peters, J. W.; Broderick, J. B. *Annu. Rev. Biochem.* **2012**, *81*, 429−450.
(25) Shepard, E. M.; McGlynn, S. E.; Bueling, A. L.; Grady-Smith, C. S.; George, S. J.; Winslow, M. A.; Cramer, S. P.; Peters, J. W.; Broderick, J. B. *Proc. Natl. Acad. Sci. U. S. A.* **2010**, *107*, 10448−10453.
(26) Driesener, R. C.; Challand, M. R.; McGlynn, S. E.; Shepard, E. M.; Boyd, E. S.; Broderick, J. B.; Peters, J. W.; Roach, P. L. *Angew. Chem., Int. Ed. Engl.* **2010**, *49*, 1687−1690.
(27) Czech, I.; Stripp, S.; Sanganas, O.; Leidel, N.; Happe, T.; Haumann, M. *FEBS Lett.* **2011**, *585*, 225−230.
(28) Czech, I.; Silakov, A.; Lubitz, W.; Happe, T. *FEBS Lett.* **2010**, *584*, 638−642.
(29) Pilet, E.; Nicolet, Y.; Mathevon, C.; Douki, T.; Fontecilla-Camps, J. C.; Fontecave, M. *FEBS Lett.* **2009**, *583*, 506−511.

(30) Kuchenreuther, J. M.; Myers, W. K.; Suess, D. L.; Stich, T. A.; Pelmenschikov, V.; Shiigi, S. A.; Cramer, S. P.; Swartz, J. R.; Britt, R. D.; George, S. J. *Science* **2014**, *343*, 424−427.
(31) Kuchenreuther, J. M.; Myers, W. K.; Stich, T. A.; George, S. J.; Nejatyjahromy, Y.; Swartz, J. R.; Britt, R. D. *Science* **2013**, *342*, 472−475.
(32) Knörzer, P.; Silakov, A.; Foster, C. E.; Armstrong, F. A.; Lubitz, W.; Happe, T. *J. Biol. Chem.* **2012**, *287*, 1489−1499.
(33) von Abendroth, G.; Stripp, S.; Silakov, A.; Croux, S.; Soucaille, S.; Girbal, L.; Happe, T. *J. Hydrogen Energy* **2008**, *33*, 6076−6081.
(34) Kuchenreuther, J. M.; George, S. J.; Grady-Smith, C. S.; Cramer, S. P.; Swartz, J. R. *PLoS One* **2011**, *6*, e20346.
(35) Kuchenreuther, J. M.; Grady-Smith, C. S.; Bingham, A. S.; George, S. J.; Cramer, S. P.; Swartz, J. R. *PLoS One* **2010**, *5*, e15491.
(36) Adamska, A.; Silakov, A.; Lambertz, C.; Rudiger, O.; Happe, T.; Reijerse, E.; Lubitz, W. *Angew. Chem., Int. Ed. Engl.* **2012**, *51*, 11458−11462.
(37) Mulder, D. W.; Ratzloff, M. W.; Shepard, E. M.; Byer, A. S.; Noone, S. M.; Peters, J. W.; Broderick, J. B.; King, P. W. *J. Am. Chem. Soc.* **2013**, *135*, 6921−6929.
(38) Silakov, A.; Kamp, C.; Reijerse, E.; Happe, T.; Lubitz, W. *Biochemistry* **2009**, *48*, 7780−7786.
(39) Kamp, C.; Silakov, A.; Winkler, M.; Reijerse, E. J.; Lubitz, W.; Happe, T. *Biochim. Biophys. Acta* **2008**, *1777*, 410−416.
(40) Wait, A. F.; Brandmayr, C.; Stripp, S. T.; Cavazza, C.; Fontecilla-Camps, J. C.; Happe, T.; Armstrong, F. A. *J. Am. Chem. Soc.* **2011**, *133*, 1282−1285.
(41) Roseboom, W.; De Lacey, A. L.; Fernandez, V. M.; Hatchikian, E. C.; Albracht, S. P. *J. Biol. Inorg. Chem.* **2006**, *11*, 102−118.
(42) Stripp, S. T.; Goldet, G.; Brandmayr, C.; Sanganas, O.; Vincent, K. A.; Haumann, M.; Armstrong, F. A.; Happe, T. *Proc. Natl. Acad. Sci. U. S. A.* **2009**, *106*, 17331−17336.
(43) Peters, J. W. *Curr. Opin. Struct. Biol.* **1999**, *9*, 670−676.
(44) Lautier, T.; Ezanno, P.; Baffert, C.; Fourmond, V.; Cournac, L.; Fontecilla-Camps, J. C.; Soucaille, P.; Bertrand, P.; Meynial-Salles, I.; Leger, C. *Faraday Discuss.* **2011**, *148*, 385−407.
(45) Finkelmann, A. R.; Stiebritz, M. T.; Reiher, M. *Chem. Sci.* **2014**, *5*, 215−221.
(46) De Gioia, L.; Zampella, G.; Fantucci, P. *Chem. Commun.* **2010**, *46*, 8824−8826.
(47) Glatzel, P.; Bergmann, U. *Coord. Chem. Rev.* **2005**, *249*, 65−95.
(48) Lancaster, K. M.; Roemelt, M.; Ettenhuber, P.; Hu, Y.; Ribbe, M. W.; Neese, F.; Bergmann, U.; DeBeer, S. *Science* **2011**, *334*, 974−977.
(49) De Groot, F.; Kotani, A. *Core Level Spectroscopy of Solids*; Taylor & Francis CRC Press: Boca Raton, FL, USA, 2008.
(50) Leidel, N.; Chernev, P.; Havelius, K. G.; Ezzaher, S.; Ott, S.; Haumann, M. *Inorg. Chem.* **2012**, *51*, 4546−4559.
(51) Hayashi, H. *Anal. Sci.* **2008**, *24*, 15−23.
(52) Glatzel, P.; Jacquamet, L.; Bergmann, U.; de Groot, F. M. F.; Cramer, S. P. *Inorg. Chem.* **2002**, *41*, 3121−3127.
(53) Izumi, Y.; Nagamori, H.; Kiyotaki, F.; Minato, T. *J. Synchrotron Radiat.* **2001**, *8*, 605−607.
(54) Wang, X.; Randall, C. R.; Peng, G.; Cramer, S. P. *Chem. Phys. Lett.* **1995**, *243*, 469−473.
(55) Grush, M. M.; Christou, G.; Haemaelaeinen, K.; Cramer, S. P. *J. Am. Chem. Soc.* **1995**, *112*, 5895−5896.
(56) Peng, G.; Wang, X.; Randall, C. R.; Moore, J. A.; Cramer, S. P. *Appl. Phys. Lett.* **1994**, *65*, 2527−2529.
(57) Wang, X.; De Groot, F.; Cramer, S. P. *Phys. Rev. B* **1997**, *56*, 4553−4564.
(58) Hamalainen, K.; Kao, C. C.; Hastings, J. B.; Siddons, D. P.; Berman, L. E.; Stojanoff, V.; Cramer, S. P. *Phys. Rev. B* **1992**, *46*, 14274−14277.
(59) Glatzel, P.; Mirone, A.; Eeckhout, S. G.; Sikora, M.; Giuli, G. *Phys. Rev. B* **2008**, *77*, 115133.1−115133.7.
(60) Lambertz, C.; Chernev, P.; Klingan, K.; Leidel, N.; Siegfridsson, K. G. V.; Happe, T.; Haumann, M. *Chem. Sci.* **2014**, *5*, 1187−1203.
(61) Lee, N.; Petrenko, T.; Bergmann, U.; Neese, F.; DeBeer, S. *J. Am. Chem. Soc.* **2010**, *132*, 9715−9727.
(62) Kirchner, B.; Wennmohs, F.; Ye, S.; Neese, F. *Curr. Opin. Chem. Biol.* **2007**, *11*, 134−141.
(63) Chandrasekaran, P.; Stieber, S. C. E.; Collins, T. J.; Que, L.; Neese, F.; DeBeer, S. *Dalton Trans.* **2011**, *40*, 11070−11079.
(64) Leidel, N.; Hsieh, C. H.; Chernev, P.; Sigfridsson, K. G.; Darensbourg, M. Y.; Haumann, M. *Dalton Trans.* **2013**, *42*, 7539−7554.
(65) Leidel, N.; Chernev, P.; Havelius, K. G.; Schwartz, L.; Ott, S.; Haumann, M. *J. Am. Chem. Soc.* **2012**, *134*, 14142−14157.
(66) Lambertz, C.; Leidel, N.; Havelius, K. G.; Noth, J.; Chernev, P.; Winkler, M.; Happe, T.; Haumann, M. *J. Biol. Chem.* **2011**, *286*, 40614−40623.
(67) Adamska-Venkatesh, A.; Krawietz, D.; Siebel, J.; Weber, K.; Happe, T.; Reijerse, E.; Lubitz, W. *J. Am. Chem. Soc.* **2014**, *136*, 11339−11346.
(68) Adams, M. W.; Johnson, M. K.; Zambrano, I. C.; Mortenson, L. E. *Biochimie* **1986**, *68*, 35−42.
(69) Knölker, H. J.; Baum, E.; Goesmann, H.; Klauss, R. *Angew. Chem., Int. Ed. Engl.* **1999**, *38*, 2064−2066.
(70) Knölker, H. J.; Heber, J.; Mahler, C. H. *Synlett* **1992**, 1002−1004.
(71) Zhao, X.; Georgakaki, I. P.; Miller, M. L.; Yarbrough, J. C.; Darensbourg, M. Y. *J. Am. Chem. Soc.* **2001**, *123*, 9710−9711.
(72) Smith, J. M.; Lachicotte, R. J.; Holland, P. L. *J. Am. Chem. Soc.* **2003**, *125*, 15752−15753.
(73) Leidel, N.; Popovic-Bijelic, A.; Havelius, K. G.; Chernev, P.; Voevodskaya, N.; Gräslund, A.; Haumann, M. *Biochim. Biophys. Acta* **2012**, *1817*, 430−444.
(74) Dau, H.; Liebisch, P.; Haumann, M. *Anal Bioanal Chem.* **2003**, *376*, 562−583.
(75) Klementiev, K. V. Freeware: http://www.cells.es/en/beamlines/bl22-claess/doc-claess_softwarexanes/view.
(76) Becke, A. D. *Phys. Rev. A* **1988**, *38*, 3098.
(77) Perdew, J. P. *Phys. Rev. B* **1986**, *33*, 8822.
(78) Schäfer, A.; Huber, C.; Ahlrichs, R. *J. Chem. Phys.* **1994**, *100*, 5829−5835.
(79) Sinnecker, S.; Rajendran, A.; Klamt, A.; Diedenhofen, M.; Neese, F. *J. Phys. Chem. A* **2006**, *110*, 2235−2245.
(80) Nicolet, Y.; de Lacey, A. L.; Vernede, X.; Fernandez, V. M.; Hatchikian, E. C.; Fontecilla-Camps, J. C. *J. Am. Chem. Soc.* **2001**, *123*, 1596−1601.
(81) Noodleman, L. *J. Chem. Phys.* **1981**, *74*, 5737−5743.
(82) Neese, F. *J. Phys. Chem. Solids* **2004**, *65*, 781−785.
(83) Lee, N.; Petrenko, T.; Bergmann, U.; Neese, F.; DeBeer, S. *J. Am. Chem. Soc.* **2010**, *132*, 9715−9727.
(84) DeBeer George, S.; Petrenko, T.; Neese, F. *Inorg. Chim. Acta* **2008**, *361*, 965−972.
(85) Li, H.; Rauchfuss, T. B. *J. Am. Chem. Soc.* **2002**, *124*, 726−727.
(86) Buhrke, T.; Löscher, S.; Lenz, O.; Schlodder, E.; Zebger, I.; Andersen, L. K.; Hildebrandt, P.; Meyer-Klaucke, W.; Dau, H.; Friedrich, B.; Haumann, M. *J. Biol. Chem.* **2005**, *280*, 19488−19495.
(87) Löscher, S.; Gebler, A.; Stein, M.; Sanganas, O.; Buhrke, T.; Zebger, I.; Dau, H.; Friedrich, B.; Lenz, O.; Haumann, M. *ChemPhysChem* **2010**, *11*, 1297−1306.
(88) Fritsch, J.; Löscher, S.; Sanganas, O.; Siebert, E.; Zebger, I.; Stein, M.; Ludwig, M.; De Lacey, A. L.; Dau, H.; Friedrich, B.; Lenz, O.; Haumann, M. *Biochemistry* **2011**, *50*, 5858−5869.
(89) Cosper, N. J.; Eby, D. M.; Kounosu, A.; Kurosawa, N.; Neidle, E. L.; Kurtz, D. M., Jr.; Iwasaki, T.; Scott, R. A. *Protein Sci.* **2002**, *11*, 2969−2973.
(90) Pollock, C. J.; Delgado-Jaime, M. U.; Atanasov, M.; Neese, F.; DeBeer, S. *J. Am. Chem. Soc.* **2014**, *136*, 9453−9463.
(91) Lubitz, W.; Reijerse, E.; van Gastel, M. *Chem. Rev.* **2007**, *107*, 4331−4365.
(92) Stripp, S.; Sanganas, O.; Happe, T.; Haumann, M. *Biochemistry* **2009**, *48*, 5042−5049.
(93) Lemon, B. J.; Peters, J. W. *Biochemistry* **1999**, *38*, 12969−12973.

(94) Brecht, M.; Gastel, M. v.; Buhrke, T.; Friedrich, B.; Lubitz, W. *J. Am. Chem. Soc.* **2003**, *125*, 13075−13083.
(95) Huotari, S.; Simonelli, L.; Giordano, V.; Rintala, A.; Sahle, C.; Hakala, M.; Glatzel, P.; Vernbeni, R.; Monaco, G. *J. Phys.: Condens. Matter* **2014**, *26*, 135501−135511.
(96) De Groot, F.; Vanko, E.; Glatzel, P. *J. Phys.: Condens. Matter* **2009**, *21*, 104207−104214.
(97) Yu, L.; Greco, C.; Bruschi, M.; Ryde, U.; De Gioia, L.; Reiher, M. *Inorg. Chem.* **2011**, *50*, 3888−3900.
(98) Tye, J. W.; Darensbourg, M. Y.; Hall, M. B. *Inorg. Chem.* **2008**, *47*, 2380−2388.
(99) Bruschi, M.; Greco, C.; Kaukonen, M.; Fantucci, P.; Ryde, U.; De Gioia, L. *Angew. Chem., Int. Ed. Engl.* **2009**, *48*, 3503−3506.
(100) Cornish, A. J.; Gartner, K.; Yang, H.; Peters, J. W.; Hegg, E. L. *J. Biol. Chem.* **2011**, *286*, 38341−38347.
(101) Dau, H.; Haumann, M. *Coord. Chem. Rev.* **2008**, *252*, 273−295.
(102) Winkler, M.; Esselborn, J.; Happe, T. *Biochim. Biophys. Acta* **2013**, *1827*, 974−985.
(103) Armstrong, F. A.; Hirst, J. *Proc. Natl. Acad. Sci. U. S. A.* **2011**, *108*, 14049−14054.
(104) Hajj, V.; Baffert, C.; Sybirna, K.; Meynial-Salles, I.; Soucaille, P.; Bottin, H.; Fourmond, V.; Leger, C. *Energy Environ. Sci.* **2014**, *7*, 715−719.
(105) Pandey, A. S.; Harris, T. V.; Giles, L. J.; Peters, J. W.; Szilagyi, R. K. *J. Am. Chem. Soc.* **2008**, *130*, 4533−4540.